Research Square

Preprints are preliminary reports that have not undergone peer review.
They should not be considered conclusive, used to inform clinical practice,
or referenced by the media as validated information.

Cholesterol metabolism sustains mitochondrial function and metastatic competence via H3K36 crotonylation-dependent ALDH1L2 activation in ovarian cancer

Shuo Chen

chenshuo0770030163.com

The Third Affiliated Hospital of Guangzhou Medical University https://orcid.org/0000-0002-5122-3656

Jia-Chen Cheng

Department of Gynecology

Mingxiu Ju

The Third Affiliated Hospital, Guangzhou Medical University

JIELIN Wang

The Third Affiliated Hospital of Guangzhou Medical University

Jing Yuan

The Third Affiliated Hospital of Guangzhou Medical University

Ai-Ping Wen

Department of Gynecology and Obstetrics

Xiang-Chun Huang

The Third Affiliated Hospital of Guangzhou Medical University https://orcid.org/0009-0002-2784-5217

Yixuan Hu

The Third Affiliated Hospital of Guangzhou Medical University

Irina Larionova

Institute of Transfusion Medicine and Immunology

Julia Kzhyshkowska

Institute of Transfusion Medicine and Immunology

Yang Zhao

Cancer Hospital of Dalian University of Technology, Cancer Hospital of China Medical University, Liaoning Cancer Hospital & Institute https://orcid.org/0000-0003-3226-8127

Article

Keywords: ovarian cancer, cholesterol metabolism, crotonylation, ALDH1L2, metastasis

Posted Date: November 25th, 2026

DOI: https://doi.org/10.21203/rs.3.rs-11520377/v1

License: This work is licensed under a Creative Commons Attribution 4.0 International License.
Read Full License

Additional Declarations:
(Not answered)

Table 3 is available in the Supplementary Files section.

Cholesterol metabolism sustains mitochondrial function and metastatic competence via H3K36 crotonylation-dependent ALDH1L2 activation in ovarian cancer

Jia-Chen Cheng[#1], MD, Ming-Xiu Ju[#2], Ph.D., Jie-Lin Wang[#1], MD, Jin Yuan[#1], MD, Ai-Ping Wen[#3], Ph.D., Xiang-Chun Huang[1], MD, Yi-Xuan Hu[1], MD, Irina Larionova[4 5], Ph.D., Julia Kzhyshkowska[4 6], Ph.D., Yang Zhao[2], Ph.D., Shuo Chen*[1], Ph.D.

[1.] Department of Obstetrics and Gynecology, Department of Gynecologic Oncology Research Office; Guangzhou Key Laboratory of Targeted Therapy for Gynecologic Oncology; Guangdong Provincial Key Laboratory of Major Obstetric Diseases; Guangdong Provincial Clinical Research Center for Obstetrics and Gynecology; Guangdong-Hong Kong-Macao Greater Bay Area Higher Education Joint Laboratory of Maternal-Fetal Medicine; The Third Affiliated Hospital, Guangzhou Medical University, Guangzhou, China.

[2.] Cancer Hospital of Dalian University of Technology, Cancer Hospital of China Medical University, Liaoning Cancer Hospital & Institute, Shenyang, Liaoning, China.

[3.] Department of Gynecology and Obstetrics, Affiliated Hospital of North Sichuan Medical College, Nanchong, Sichuan, China.

[4.] Laboratory of Translational Cellular and Molecular Biomedicine, National Research Tomsk State University, Tomsk, Russia.

[5.] Laboratory of Molecular Therapy of Cancer, Cancer Research Institute, Tomsk National Research Medical Center, Russian Academy of Sciences, Tomsk, Russia.

[6.] Institute of Transfusion Medicine and Immunology, Institute for Innate Immunoscience (MI3), Medical Faculty Mannheim, Heidelberg University, Mannheim, Germany.

# These authors contributed equally to this work

*Correspondence to:

Shuo Chen, Email: chenshuo077003@163.com; Address: No.63 Duobao Road, Liwan District, Guangzhou City, Guangdong Province, P.R. China

Abstract

Mitochondrial redox homeostasis is critical for cancer cell survival during metastasis, yet the systemic signals sustaining this balance remain unclear. Here we identify a cholesterol-driven metabolic relay that controls mitochondrial redox through enhancer-directed epigenetic activation of ALDH1L2. ALDH1L2 catalyzes 10-formyltetrahydrofolate deformylation to regenerate tetrahydrofolate with concomitant NADPH production, sustaining mitochondrial membrane potential and suppressing intracellular ROS. Mechanistically, profiling of 17 short-chain acyl-CoAs revealed that crotonyl-CoA accumulated most prominently in highly invasive ovarian cancer cells, providing substrate for locus-specific histone H3 lysine 36 crotonylation (H3K36cr) at ALDH1L2 regulatory elements. This modification facilitated YY1 occupancy, driving ALDH1L2 expression. Clinically, serum cholesterol was significantly elevated in advanced-stage (FIGO III–IV) versus early-stage (FIGO I–II) ovarian cancer patients, and exogenous cholesterol enhanced cell proliferation, migration, and invasion. Genetic disruption of H3K36 crotonylation via an H3K36R mutant impaired ALDH1L2 expression and suppressed tumor growth in vivo. Pharmacological inhibition of cholesterol synthesis with simvastatin reduced H3K36cr deposition, elevated intracellular ROS, depolarized mitochondria, and suppressed tumor growth in xenograft and patient-derived organoid models. These findings establish a cholesterol–crotonyl-CoA–H3K36cr–ALDH1L2 axis linking systemic lipid metabolism to mitochondrial redox control, revealing a vulnerability that may be exploited therapeutically in advanced ovarian cancer.

Keywords: ovarian cancer; cholesterol metabolism; crotonylation; ALDH1L2; metastasis

Graphical abstract

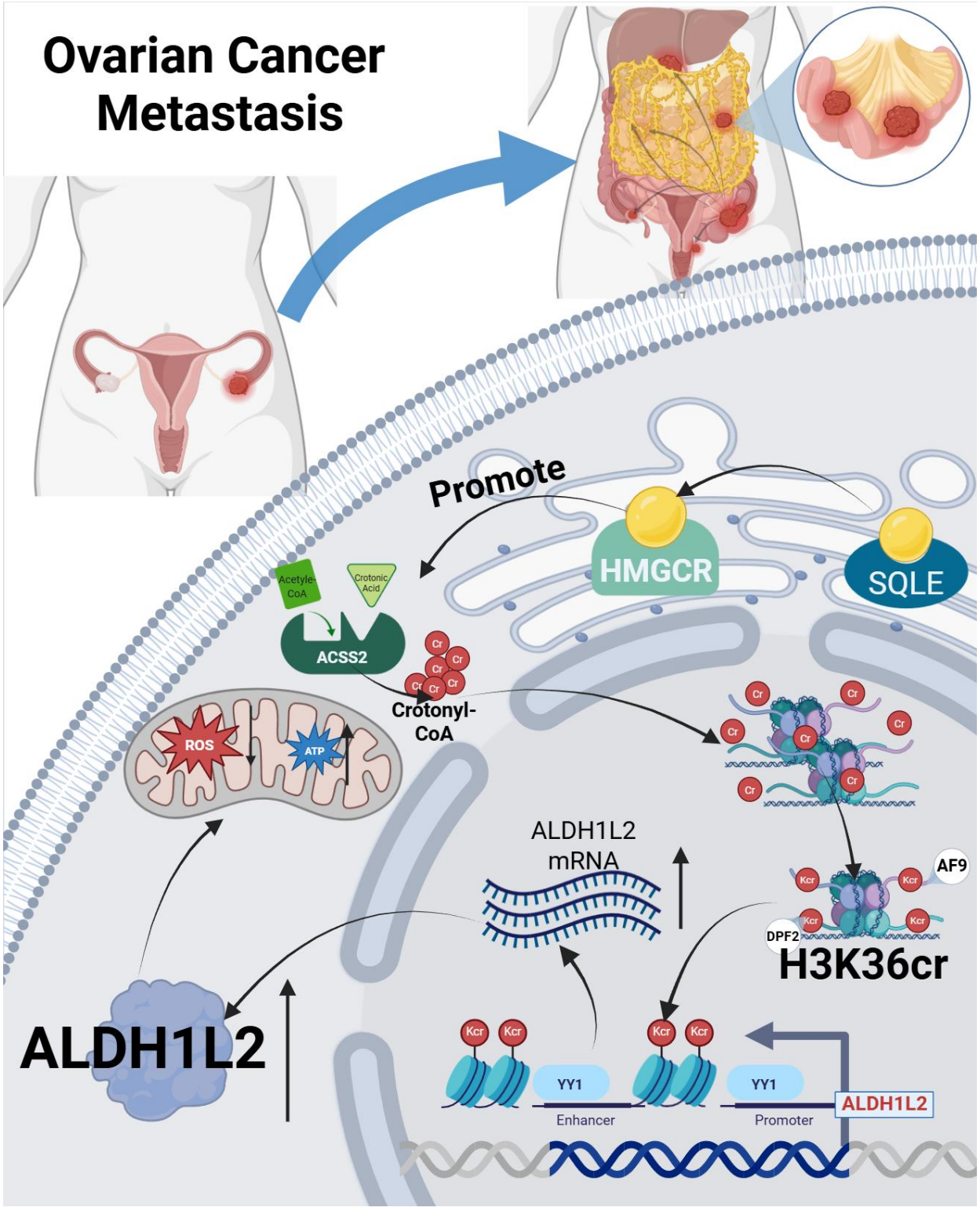

1. Introduction

Ovarian cancer (OC) remains one of the most lethal gynecological malignancies, characterized by persistently high mortality rates worldwide [1]. Although cytoreductive surgery, platinum/taxane-based chemotherapy, and poly (ADP-ribose) polymerase (PARP) inhibitor maintenance therapy has improved outcomes for specific patient subsets, overall survival remains highly unsatisfactory [2] [3]. A major driving factor for this dismal prognosis is that the vast majority of patients present with extensive peritoneal dissemination, lymphatic spread, or distant organ metastases at initial diagnosis, which severely limits therapeutic efficacy. Therefore, elucidating the underlying molecular mechanisms of OC metastasis represents an urgent clinical imperative.

Consistent with emerging reports across various malignancies, cholesterol metabolism is increasingly recognized as a critical determinant of metastatic competence [4] [5] [6]. As a core structural component of the lipid bilayer, hyperactivated cholesterol biosynthesis not only fulfills the immense demand for membrane expansion during tumor invasion but also generates diverse metabolic intermediates [7] [8] [9]. These intermediates can serve as pivotal signaling molecules or donors for epigenetic modifications, directly driving the evolution of malignant phenotypes [10] [11]. However, the precise role and downstream molecular cascade of cholesterol metabolism in OC—particularly during metastatic progression—remain insufficiently defined. By systematically analyzing clinical biochemical profiles, cohorts from the NHANES database, and single-cell RNA sequencing (scRNA-seq) datasets of paired primary and metastatic OC lesions, we observed a marked enrichment of cholesterol metabolic programs specifically in metastatic foci.

From our transcriptomic profiling, ALDH1L2—encoding a mitochondrial aldehyde dehydrogenase that regulates one-carbon metabolism, redox balance, and mitochondrial membrane potential [12] [13] [14] [15]-emerged among the most differentially expressed genes in cholesterol-enriched conditions. ALDH1L2 catalyses 10-formyltetrahydrofolate deformylation to

regenerate tetrahydrofolate with concomitant NADPH production, positioning it at the intersection of folate metabolism and oxidative stress control. Recent studies have implicated ALDH1L2 in cancer cell migration and metabolic adaptation [13,14], yet whether and how cholesterol flux regulates ALDH1L2 transcription, and whether ALDH1L2 functionally mediates cholesterol-driven metastatic phenotypes in ovarian cancer, remain open questions.

The robust transcriptional activation of metabolic effectors such as ALDH1L2 requires coordinated regulation in cis—through enhancers, transcription factors, and permissive chromatin states [16] [17] [18]. Emerging evidence indicates that metabolic reprogramming can directly reshape the chromatin landscape via metabolite-driven histone modifications, with the acyl-CoA pool serving as a key biochemical interface [19]. Histone lysine crotonylation (Kcr) is a transcription-permissive modification whose acyl donor, crotonyl-CoA, fluctuates with short-chain acyl flux and fatty acid β-oxidation [20]and has been implicated in tumour initiation and metastatic plasticity [21] [22, 23]. However, whether cholesterol metabolism—as a master regulator of lipid flux—alters the crotonyl-CoA reservoir to drive site-specific Kcr deposition at metastasis-relevant gene loci has not been investigated.

Here, by integrating multi-omics analyses (RNA-seq, ATAC-seq, and targeted metabolomics) with functional epigenetics, we tested whether cholesterol reprograms chromatin accessibility and histone crotonylation at the ALDH1L2 locus. We identify a signalling cascade in which cholesterol-driven crotonyl-CoA expansion deposits H3K36cr at ALDH1L2 enhancers, facilitates YY1 occupancy, and activates a mitochondrial metabolic program that sustains ovarian cancer aggressiveness. Pharmacological blockade with simvastatin disrupts this axis, revealing a metabolic–epigenetic vulnerability.

2. Materials and methods

2.1 Clinical Specimens and Immunohistochemistry (IHC)

Paired primary and metastatic ovarian cancer tissues were obtained from the affiliated hospital of Guangzhou Medical University with written informed consent and institutional ethical approval (No. 2025-023), in strict accordance with the Declaration

of Helsinki. Formalin-fixed, paraffin-embedded (FFPE) sections (4 μm) were deparaffinized, rehydrated, and subjected to microwave-assisted antigen retrieval. Following endogenous peroxidase quenching (3% H2O2) and blocking (5% BSA), the sections were incubated overnight at 4°C with primary antibodies against HMGCR (Cat#13533-1-AP, 1:200), SQLE (Cat#12544-1-AP, 1:200), and ALDH1L2 (Cat#21391-1-AP, 1:200), all sourced from Proteintech (Wuhan, China). Subsequently, the slides were incubated with an HRP-conjugated secondary antibody for 1 hour at room temperature, visualized using a DAB chromogen kit, and counterstained with hematoxylin. Immunoreactivity was independently evaluated by two blinded pathologists using an H-score system (ranging from 0 to 300), calculated by multiplying the staining intensity score (0–3) by the percentage of positively stained cells (0–100%).2.2 Omics & Bioinformatics

2.2 scRNA-seq Data Processing and Analysis

The public single-cell RNA sequencing (scRNA-seq) dataset GSE222557 was acquired from the Gene Expression Omnibus (GEO) database. To ensure the reliability of downstream analyses, stringent quality control (QC) was performed to filter out low-quality cells. Specifically, cells were retained if they met the following criteria: the number of expressed genes (nFeature_RNA) was fewer than 10,000, the total unique molecular identifiers (nCount_RNA) were fewer than 40,000, and the proportion of mitochondrial gene expression was less than 15%. Subsequent data normalization, dimensionality reduction, and unsupervised clustering were executed using the Seurat R package (version 4.3.0) [24]. For visualization, Uniform Manifold Approximation and Projection (UMAP) was applied utilizing the first 24 principal components (PCs). Furthermore, complex cell-cell communication networks and signaling pathway interactions among distinct cell subpopulations were inferred and visualized utilizing the CellChat R package[25].

2.3 ATAC-seq Library Preparation and Data Analysis

To map genome-wide chromatin accessibility, ATAC-seq libraries were generated from 50,000 viable ovarian cancer cells. Following nuclei isolation in cold lysis buffer (10 mM Tris-HCl pH 7.4, 10 mM NaCl, 3 mM MgCl2, 0.1% IGEPAL CA-630) for 10 min, Tn5 transposition was performed using the Nextera DNA Library Preparation Kit (Illumina) at 37°C for 30 min. Amplified and bead-purified libraries were evaluated on an Agilent 2100 Bioanalyzer and sequenced on an Illumina NovaSeq 6000 platform (PE150 strategy) by Novogene (Beijing, China). For bioinformatics analysis, raw reads

were trimmed with Trimmomatic and aligned to the human reference genome (GRCh38/hg38) using Bowtie2. After filtering mitochondrial reads, multi-mappers, and PCR duplicates via Picard and SAMtools, chromatin accessibility peaks were called using MACS2 and annotated with the ChIPseeker R package. Finally, de novo motif enrichment within differential peaks was conducted using HOMER to specifically interrogate potential YY1 binding sites at the ALDH1L2 promoter [26] [27] [28].

2.4 Targeted Metabolomics Analysis of Acyl-CoAs

For targeted metabolomic profiling of 18 specific intracellular acyl-CoAs, metabolites were extracted from cultured ovarian cancer cells using a cold methanol/chloroform/water phase-separation method, vacuum-dried, and reconstituted in 50 μL of methanol/water (3:2, v/v). The extracts were analyzed using a Vanquish Core HPLC coupled to a Q Exactive HF-X Orbitrap mass spectrometer (Thermo Fisher Scientific). Chromatographic separation was performed on a Waters CSH C18 column (2.1 × 100 mm, 1.7 μm) at 40°C, employing a gradient elution of 10 mM aqueous ammonium acetate and acetonitrile at a flow rate of 0.40 mL/min. Data acquisition was executed in positive electrospray ionization (ESI+) and Full MS/dd-MS2 scanning modes with optimized source parameters (3200 V spray voltage; 320°C capillary temperature). Finally, the target metabolites—including acetyl-CoA and crotonyl-CoA—were qualitatively identified by matching high-resolution spectra against an in-silico MS/MS library, and absolutely quantified using linear regression derived from serially diluted external standard calibration curves (10–1000 ng/mL).

2.5 Establishment of a highly invasive A2780-PM (Post-Migration) subline by serial Transwell selection

A 24-well Transwell invasion system (8-μm pore size) pre-coated with Matrigel (1:8 dilution) was used for iterative selection. In each round, 1*10^4 A2780 cells were seeded in the upper chamber in serum-free medium, and complete medium containing 10% FBS was placed in the lower chamber as chemoattractant. After 24 h, invaded cells on the lower membrane side were collected, expanded to logarithmic growth, and used as the input for the next round. A total of 5–8 rounds were performed until a stable increase in invasion was observed; the subline was designated A2780-PM(Post-Migration) [29] [30]. The procedural framework followed established in vitro migration/invasion methodologies.

2.6 Measurement of Cellular Energy Metabolism (OCR and ECAR)

To assess mitochondrial respiration and glycolytic capacity, the cellular oxygen consumption rate (OCR) and extracellular acidification rate (ECAR) were evaluated using specific commercial assay kits (Elabscience Biotechnology Co., Ltd., Wuhan, China) according to the manufacturer's protocols. Briefly, human ovarian cancer cells were seeded into 96-well culture plates (1×10^4 cells/well) and allowed to adhere overnight. For the OCR measurement, the standard medium was replaced with an assay buffer containing an oxygen-sensitive fluorescent probe, and the wells were immediately sealed with mineral oil to prevent ambient oxygen diffusion prior to continuous kinetic fluorescence recording. In parallel, for the ECAR assay, cells were incubated with an extracellular acidification buffer containing a pH-sensitive indicator to kinetically monitor dynamic signal changes driven by cellular lactate production and proton efflux. Ultimately, both OCR and ECAR kinetic measurements were normalized to the total cellular protein concentration of the corresponding wells, as determined by the BCA protein assay, to eliminate variations caused by disparate cell numbers.

2.7 Integration of transcription factor (TF) and enhancer resources

Potential upstream transcription factors (TFs) were systematically screened and identified through an integrative analysis of existing literature and public regulatory databases, specifically utilizing the Cistrome Data Browser[31], hTFtarget[32], and HumanTFDB[33]. For genomic regulatory annotations, active enhancer landscapes were mapped according to the FANTOM5 consortium atlas[34]. To pinpoint specific TF binding events, motif enrichment and digital footprinting analyses were performed exclusively within the accessible chromatin regions (ATAC-seq peaks) utilizing the HOMER algorithmic suite[35].

2.8 3D Tumor Spheroid and Patient-Derived Organoid (PDO) Culture

To bridge the gap between in vitro 2D cultures and in vivo physiology, 3D tumor spheroids and patient-derived organoids (PDOs) were constructed for pharmacological evaluation. Single-cell suspensions, prepared from cultured ovarian cancer cells or primarily isolated patient tumor tissues by mechanical and enzymatic dissociation, were resuspended in cold Matrigel (Yeasen Biotechnology) and seeded as 30-40 μL domes into pre-warmed 24-well plates. Following a 30-minute polymerization at 37°C, domes were overlaid with specialized organoid culture medium (Advanced DMEM/F12 supplemented with B27, epidermal growth factor, fibroblast growth factor, and the ROCK inhibitor Y-27632), with medium refreshed every 3 days. Mature organoids were then treated with indicated drugs (e.g., simvastatin,

cholesterol). Morphological alterations and diameters were monitored via inverted phase-contrast microscopy, and overall cell viability and ATP content were quantified using a luminescent 3D cell viability assay kit, with signals recorded by a microplate reader.

2.9 Exogenous Drug Preparation and Cell Treatment

To investigate the effects of pharmacological intervention and lipid metabolism, ovarian cancer cells were treated with simvastatin and cholesterol. Simvastatin (MedChemExpress, a HMG-CoA reductase inhibitor) and cholesterol (MedChemExpress) were prepared as high-concentration stock solutions by dissolving in dimethyl sulfoxide (DMSO) and stored at -20°C. For cellular assays, these stocks were freshly diluted in complete culture medium to working concentrations of 50 nM for simvastatin and 50 μg/mL for cholesterol. The final DMSO concentration was maintained below 0.1% (v/v) across all groups to rule out vehicle-induced cytotoxicity. After overnight adherence in multi-well plates, cells were treated with the drug-containing medium for durations typically ranging from 24 to 48 hours, optimized based on downstream functional assay requirements.

3. Results

3.1 Cholesterol metabolism is enriched in metastatic ovarian cancer tissues

We first analyzed the clinical biochemical data from our institution. We observed that serum total cholesterol (TC) levels were significantly elevated in patients with FIGO stage III-IV ovarian cancer (**Figure 1A, Table 1**). Consistently, low-density lipoprotein cholesterol (LDL), a lipid component directly related to cholesterol metabolism, was also significantly increased (**Figure 1A, Table 2,** patients are listed in **Table S1**). These findings prompted us to hypothesize that the proliferation and metastasis of ovarian cancer are closely associated with cholesterol metabolism dysregulation. To investigate the correlation between ovarian cancer and blood biochemical markers, we initially analyzed data from the NHANES database and found that TC exhibited the highest correlation with ovarian cancer (**Figure 1B**). Serum TC and LDL-C levels in ovarian cancer patients were significantly higher than those in healthy controls (**Figure S1A**).

To further validate our hypothesis, we analyzed a single-cell RNA sequencing (scRNA-seq) dataset from the GEO database (GSE222557; patient registration numbers are listed in Table S2). After quality control, unsupervised clustering, and cell annotation using key marker genes (**Figure S1B**), the UMAP plot clearly delineated the major cell populations (**Figure 1C**). We then evaluated the proportions of various cell types in primary and metastatic lesions (**Figure S1D**). Differential gene expression analysis between primary and metastatic tumor cells, combined with Gene Ontology Biological Process (GO:BP) enrichment analysis, revealed a significant enrichment of cholesterol metabolism pathways (**Figure 1D**). Furthermore, within a predefined 12-gene set central to cholesterol metabolism (SREBF1, SREBF2, INSIG1, LDLR, HMGCR, HMGCS1, IDI1, FDFT1, SQLE, MVK, PMVK, and MVD), most genes were significantly upregulated in metastatic tumor cells (**Figure 1F**).

Orthogonal validation using our institutional samples further supported these findings. Immunohistochemistry (IHC) staining showed that the protein expression levels of HMGCR and SQLE, the rate-limiting enzymes in cholesterol biosynthesis, were markedly increased in metastatic lesions (**Figure 1E**). We continued to mine the scRNA-seq data and utilized CellChat analysis, which revealed active cell-cell communication between tumor cells and other cell populations in metastatic lesions (Figure S1C). Notably, metastatic tumor cells exhibited highly significant

communication with endothelial cells via the vascular endothelial growth factor (VEGF) pathway (**Figure 1H-I**). Furthermore, module scoring of metastatic tumor cells based on cholesterol metabolism-related genes showed that tumor cells with high cholesterol metabolism scores displayed stronger interactions with vascular endothelial cells compared to those with low scores (**Figure S1E-F**). Collectively, these multi-omics and histopathological data support a model in which cholesterol metabolism is significantly upregulated in metastatic ovarian cancer, carrying important clinical, pathological, and prognostic significance.

3.2 Establishment and characterization of a highly invasive ovarian cancer subline

To better explore how metabolic changes affect the metastatic potential of ovarian cancer cells, we selected the A2780 cell line. Guided by MetMap[36], A2780 is prone to metastasize to the cholesterol-rich liver. By adding exogenous cholesterol to the lower chamber of a Transwell apparatus and performing multiple rounds of invasion screening, we successfully established a highly invasive subline, A2780-Post Membrane (A2780-PM) (**Figure 2A**). F-actin staining using Actin-Tracker revealed that A2780-PM cells formed more pseudopodia-like structures (**Figure 2B**). Consistently, Western blotting confirmed higher expression levels of proteins associated with primary site shedding and metastasis-related pseudopodia formation in A2780-PM cells (**Figure 2C**). Transwell assays demonstrated that the A2780-PM subline possessed stronger migration and invasion capabilities (**Figure 2D**). CCK-8 assays indicated its enhanced proliferation ability (**Figure 2E**).

To further validate its phenotype in vivo, orthotopic xenograft mouse models showed that A2780-PM cells possessed stronger in vivo proliferation and local invasion capabilities, forming massive tumor lesions around the murine ovaries (**Figure 2F**). Subcutaneous xenograft models also revealed that A2780-PM exhibited a significantly faster in vivo tumor growth rate compared to the parental cell line (**Figure 2G**).

Subsequently, we measured the total intracellular cholesterol content in A2780-PM cells. The total cholesterol accumulation was significantly higher than that in the parental cells (**Figure 2H**). Western blotting and qPCR assays further confirmed that the mRNA and protein expression levels of key cholesterol metabolic enzymes, HMGCR and SQLE, were significantly upregulated in A2780-PM cells compared to parental cells (**Figure 2I-J**). HUVEC tube formation assays revealed that A2780-PM

cells had a significantly enhanced ability to promote angiogenesis, which is consistent with the characteristics of ovarian cancer metastatic lesions (**Figure 2K**). Flow cytometry and confocal microscopy using exogenous fluorescently labeled cholesterol (BODIPY-Cholesterol) [37] demonstrated that A2780-PM cells could uptake and accumulate free cholesterol from the environment more rapidly and efficiently (**Figure 2L-M**).

3.3 Cholesterol metabolic reprogramming promotes rapid growth and metastatic phenotypes

Based on the rapid cholesterol accumulation ability observed in A2780-PM cells, we found that parental A2780 cells also exhibited cholesterol accumulation upon cholesterol exposure (**Figure 3A**). To mimic this metabolic alteration, we subjected parental A2780 cells to long-term culture with exogenous cholesterol supplementation. Actin-Tracker staining revealed that A2780 cells chronically exposed to exogenous cholesterol similarly displayed highly malignant phenotypes, such as increased pseudopodia (**Figure 3B**). EdU incorporation assays showed that exogenous cholesterol significantly promoted A2780 cell proliferation. Conversely, knocking down the key cholesterol metabolic enzymes HMGCR or SQLE in the highly invasive A2780-PM cells markedly inhibited cell proliferation (**Figure 3C**). CCK-8, Transwell, and scratch wound healing assays also confirmed that exogenous cholesterol supplementation comprehensively enhanced cell proliferation, invasion, and migration. Targeted interference with cholesterol metabolism effectively suppressed these malignant biological behaviors (**Figure 3D-F**). Furthermore, flow cytometry combined with Annexin V apoptosis staining analysis indicated that the addition of exogenous cholesterol reduced the basal apoptosis level of cells. In contrast, blocking cholesterol metabolism led to a significant increase in the cell apoptosis rate (**Figure 3G**).

3.4 Cholesterol exerts pro-tumoral functions by regulating ALDH1L2

To elucidate the molecular mechanisms by which cholesterol metabolic reprogramming drives the malignant progression of ovarian cancer, we performed RNA-seq analysis on long-term cholesterol-cultured A2780 cells and their parental counterparts (**Figure 4A**). We intersected the differentially expressed genes from sequencing with lipid metabolism-related gene sets from the GO-BP database. Among the candidate genes, ALDH1L2 emerged as a prominent cholesterol metabolism-associated effector with marked differential expression and was therefore selected for further investigation (**Figure 4B**). Joint analysis based on the TCGA and GTEx

databases revealed that ALDH1L2 expression levels in ovarian cancer tissues were significantly higher than those in normal tissues (**Figure 4C**) (13–16). Kaplan–Meier survival analysis further showed that high ALDH1L2 expression was closely associated with poorer overall survival in patients with ovarian cancer (**Figure 4D**).

Western blotting and RT–qPCR confirmed that ALDH1L2 mRNA and protein expression were significantly upregulated in A2780-PM cells compared with parental A2780 cells (primer sequences are listed in Table S3). In addition, ALDH1L2 expression was increased after cholesterol stimulation in A2780 cells, whereas knockdown of cholesterol synthesis-related enzymes, including HMGCR and SQLE, reduced ALDH1L2 expression in A2780-PM cells (**Figure 4E-F**). Immunofluorescence assays further demonstrated stronger ALDH1L2 protein expression in A2780-PM cells than in parental A2780 cells (Figure 4G). Consistently, IHC staining of paired clinical specimens from our center showed that ALDH1L2 expression was elevated in metastatic lesions compared with matched primary ovarian cancer tissues (**Figure 4H**).

ALDH1L2 is a mitochondrial metabolic enzyme involved in the regulation of mitochondrial redox homeostasis and energy metabolism. Multicolor immunofluorescence co-staining using BODIPY-cholesterol, MitoTracker and ALDH1L2 antibodies revealed evident spatial co-localization among cholesterol signals, mitochondria and ALDH1L2 in A2780-PM cells (**Figure 4I**). These findings suggest that cholesterol flux may be functionally linked to mitochondrial metabolism through ALDH1L2, thereby providing metabolic support for the malignant phenotypes of ovarian cancer cells.

Therefore, we overexpressed ALDH1L2 in parental A2780 cells and knocked down ALDH1L2 in highly invasive A2780-PM cells to verify its functions. Colony formation and CCK-8 assays demonstrated that ALDH1L2 overexpression conferred stronger proliferation capacity, whereas ALDH1L2 knockdown impaired proliferation (**Figure S2A-B**). Transwell and scratch assays showed that ALDH1L2 overexpression enhanced cell invasion and migration, while ALDH1L2 knockdown significantly attenuated these capabilities (**Figure S2C-D**). Annexin V apoptosis assays revealed that the apoptosis rate of A2780-PM cells significantly increased after ALDH1L2 knockdown (**Figure S2E**). This fully demonstrates that ALDH1L2 is a key factor in maintaining the malignant phenotypes of ovarian cancer.

Subsequently, we evaluated the specific effects of ALDH1L2 on mitochondrial metabolism. Flow cytometric detection of ROS levels showed that ALDH1L2 knockdown in A2780-PM cells led to a significant increase in intracellular ROS accumulation (**Figure 4J**). JC-1 staining demonstrated that ALDH1L2 knockdown decreased the mitochondrial membrane potential of A2780-PM cells (**Figure 4K**). Oxygen consumption rate (OCR) and extracellular acidification rate (ECAR) measurements further confirmed that ALDH1L2 knockdown markedly impaired the metabolic activity of A2780-PM cells (**Figure 4L**).

In vivo mouse xenograft models further confirmed the tumor-promoting role of ALDH1L2. In the subcutaneous xenograft model, ALDH1L2 knockdown markedly reduced the volume of A2780-PM tumors and significantly slowed tumor growth (**Figure 4M**). Consistently, in the intraperitoneal xenograft model, longitudinal in vivo bioluminescence imaging showed that ALDH1L2 knockdown substantially suppressed intraperitoneal tumor progression compared with the vehicle control group (**Figure 4N**). Collectively, these findings establish ALDH1L2 as a critical mitochondrial enzyme that links cholesterol metabolic reprogramming with cellular energy dynamics, thereby fueling ovarian cancer malignant progression and highlighting ALDH1L2-related metabolic vulnerability as a potential therapeutic target.

3.5 Cholesterol regulates ALDH1L2 transcription by activating promoter transcription factors and chromatin accessibility

Previous qPCR assays indicated that ALDH1L2 is primarily regulated at the transcriptional level. To investigate the specific epigenetic mechanisms by which cholesterol metabolic reprogramming affects ALDH1L2 transcription, we performed ATAC-seq on A2780 cells cultured long-term with or without cholesterol supplementation. The ATAC-seq datasets showed extensive overlap of accessible chromatin regions between control and cholesterol-treated cells, while cholesterol exposure also generated a large number of condition-specific accessible regions (**Figure S3A**). Differential accessibility analysis further revealed widespread cholesterol-induced chromatin remodeling, with both gained and lost accessible peaks detected across the genome (**Figure S3B**). Genomic annotation showed that the overall distribution of accessible peaks across promoters, introns, exons, downstream regions and distal intergenic regions was comparable between control and cholesterol-treated cells (**Figure S3C**), indicating that cholesterol did not globally alter the genomic category distribution of open chromatin regions.

Functional enrichment analysis of differential accessible regions demonstrated that cholesterol-associated chromatin remodeling was enriched in biological processes related to small GTPase-mediated signal transduction, cell junction assembly, morphogenesis, actin filament organization and cell projection organization, as well as KEGG pathways including PI3K–Akt signaling, MAPK signaling, calcium signaling, focal adhesion, regulation of actin cytoskeleton and Rap1 signaling (**Figure S3D**). These pathways are closely linked to cytoskeletal remodeling, cell adhesion, migration and invasive progression. Moreover, enhancer ranking analysis identified a subset of high-signal enhancer elements in cholesterol-treated cells, supporting the notion that cholesterol metabolic reprogramming reshapes distal regulatory landscapes (**Figure S3E**).

Consistent with these global chromatin changes, ATAC-seq analysis revealed that cholesterol treatment induced a genome-wide increase in chromatin accessibility (**Figure 5A–C**). In-depth annotation of ALDH1L2-related peaks further showed that the chromatin accessibility of the ALDH1L2 locus was significantly increased following cholesterol treatment (**Figure 5D**).

In addition to promoters, distal transcriptional regulatory elements also profoundly affect mRNA transcription levels. ATAC-seq data annotation indicated a general increase in the openness of enhancer regions after cholesterol treatment (**Figure 5E**). Because enhancers act synergistically with specific transcription factors (TFs), we combined multiple TF databases, including Cistrome, GTRD, hTFtarget and HumanTFDB, with ATAC-seq motif analysis. We ultimately identified SREBP1, IRF-1, YY1 and MYC as candidate transcription factors regulating ALDH1L2 (**Figure 5F**). We individually knocked down these four TFs in A2780-PM cells. The results showed that, compared with the si-NC control group, YY1 knockdown caused the most pronounced decrease in ALDH1L2 protein expression (**Figure 5G**). RT–qPCR further confirmed that YY1 knockdown significantly inhibited ALDH1L2 mRNA transcription. Meanwhile, correlation analysis based on the TCGA ovarian cancer cohort also demonstrated a significant positive co-expression correlation between YY1 and ALDH1L2 in clinical samples (**Figure 5H**).

To verify the direct transcriptional activation effect of YY1 on the ALDH1L2 promoter, we constructed a luciferase reporter plasmid containing the ALDH1L2 promoter region (**Figure 5I**). Dual-luciferase reporter assays showed that YY1 overexpression

significantly enhanced the transcriptional activity of this promoter (**Figure 5J**). Subsequent ChIP–qPCR assays directly confirmed that YY1 was highly enriched at the ALDH1L2 promoter region (**Figure 5K**).

3.6 Cholesterol activates proximal enhancers of the ALDH1L2 promoter to promote transcription

Further mining of the ATAC-seq data revealed that cholesterol treatment not only opened the promoter but also significantly increased the accessibility of multiple potential enhancer sites within the ALDH1L2 regulatory region (**Figure 6A**). By integrating the FANTOM5 enhancer database, we identified three proximal enhancer elements (designated E1, E2, and E3) upstream of the ALDH1L2 promoter (**Figure 6B**). After individually or jointly knocking out E1-E3 using CRISPR-Cas9 technology in A2780-PM cells, qPCR and Western blotting results showed that ALDH1L2 mRNA and protein expression levels were significantly suppressed (**Figure 6C-D**). ChIP-qPCR analysis demonstrated that all three enhancer regions could recruit the transcription factor YY1 (**Figure 6E**). However, after knocking out E1-E3, the enrichment of YY1 at the ALDH1L2 core promoter region was drastically reduced (**Figure 6F**), indicating that enhancers synergistically activate transcription by promoting YY1 recruitment.

Functional phenotypic rescue assays demonstrated that knocking out E1-E3 (especially joint knockout) using CRISPR-Cas9 significantly attenuated cell proliferation, invasion, and migration capabilities (**Figure 6G-I**). Flow cytometric apoptosis detection also found that enhancer deletion led to a significant increase in the cell apoptosis rate (**Figure 6J**).

3.7 Cholesterol reprogramming regulates ALDH1L2 transcription via histone H3K36 crotonylation

Histone post-translational modifications (PTMs) play a decisive role in epigenetic transcriptional regulation, and these modifications highly depend on various acyl-CoAs as substrate donors[22]. We quantitatively measured the relative abundance of 17 short-chain acyl-CoAs in parental A2780 and A2780-PM cells via targeted metabolomics analysis. The results were striking: the pool size of crotonyl-CoA in A2780-PM cells expanded most significantly (**Figure 7A**). Western blotting and ELISA quantitative assays confirmed that intracellular crotonyl-CoA levels were significantly elevated in A2780-PM cells and cholesterol-stimulated A2780 cells (**Figure 7B**). This was accompanied by an overall upregulation of pan-crotonylation (Pan-Kcr) modification levels in the whole cell (**Figure 7C-D**). Notably, as a comparison, histone

acetylation levels, which typically compete with crotonylation, did not change significantly (**Figure 7E**).

ACSS2 is the key metabolic enzyme that catalyzes the generation of crotonyl-CoA. AF9, containing a YEATS domain, and DPF2, containing a double PHD domain, are known key crotonylation "readers" that can recognize Kcr modifications and convert them into transcriptional signals [38] [39] [40]. Knocking down ACSS2 or the reader proteins AF9/DPF2 in A2780-PM and cholesterol-treated A2780 cells effectively reduced ALDH1L2 mRNA and protein expression levels (**Figure 7F-G**).

To identify the specific crotonylation sites among the core histones (H2A, H2B, H3, H4), we performed co-immunoprecipitation (Co-IP) assays and found that histone H3 crotonylation increased most markedly under cholesterol-enriched conditions (**Figure 7H**). Further site-specific Western blotting confirmed that the crotonylation of lysine 36 on histone H3 (H3K36cr) showed the most dramatic upregulation in A2780-PM and cholesterol-treated A2780 cells (**Figure 7I**).

ChIP-qPCR results confirmed the enrichment of the H3K36cr modification signal at the ALDH1L2 locus (**Figure 7J**). More importantly, in A2780-PM and cholesterol-treated A2780 cells, H3K36cr was not only highly enriched at the core promoter region of ALDH1L2 (**Figure 7K**) but also exhibited a strong enrichment signal at its proximal enhancer regions, E1-E3 (**Figure 7L**).

3.8 Modulating histone crotonylation inhibits the malignant phenotypes of ovarian cancer

Based on the above findings, we hypothesized that interfering with histone H3K36 crotonylation could reverse the malignant phenotypes of ovarian cancer. To this end, we constructed an H3K36R point mutation plasmid, in which lysine at position 36 of histone H3 was mutated to arginine, thereby preventing acylation at this residue (**Figure 8A**). Western blotting and Co-IP assays confirmed that transfection with the H3K36R mutant plasmid markedly reduced H3K36 crotonylation levels in A2780-PM cells (**Figure 8B**).

To further evaluate the functional consequence of H3K36 crotonylation blockade in vivo, we established an intraperitoneal A2780-PM tumor model using cells expressing either the vehicle control or H3K36R mutant plasmid. Longitudinal bioluminescence imaging showed that H3K36R markedly suppressed intraperitoneal tumor progression compared with the vehicle control group (**Figure 8C**). Consistently, subcutaneous

xenograft analysis demonstrated that H3K36R significantly reduced tumor burden, as reflected by smaller excised tumors and decreased tumor volume (**Figure 8E**). Tumor growth curves based on tumor diameter further confirmed the inhibitory effect of H3K36R on A2780-PM tumor growth, and this suppression could not be rescued by exogenous cholesterol supplementation (**Figure S4B**).

At the molecular level, the H3K36R-induced crotonylation defect was accompanied by a marked decrease in ALDH1L2 expression. Western blotting confirmed that H3K36R substantially reduced ALDH1L2 protein levels in A2780-PM cells, and this inhibitory effect was not reversed by additional cholesterol treatment (**Figure 8D**). In vitro CCK-8 assays further showed that H3K36R significantly impaired the proliferative capacity of A2780-PM cells (**Figure S4A**). Together, these results indicate that H3K36 crotonylation is required for maintaining ALDH1L2 expression and cholesterol-driven malignant progression in ovarian cancer.

3.9 Simvastatin inhibits the malignant phenotypes of ovarian cancer

Simvastatin, a classic inhibitor of HMGCR, can effectively block endogenous cholesterol synthesis at its source. We first evaluated the half-maximal inhibitory concentration of simvastatin in A2780-PM cells and determined an IC50 of 51.09 nM (**Figure 8F; Figure S4C**), suggesting that A2780-PM cells are sensitive to pharmacological inhibition of cholesterol synthesis.

Functionally, simvastatin treatment markedly suppressed the malignant phenotypes of A2780-PM cells. Colony formation assays showed that simvastatin reduced clonogenic growth (**Figure S4D**). Flow cytometric apoptosis analysis demonstrated that simvastatin significantly increased apoptosis in A2780-PM cells (**Figure S4E**). In addition, scratch assays showed that simvastatin impaired the migratory capacity of A2780-PM cells (**Figure S4F**), while Transwell assays confirmed that simvastatin significantly inhibited cellular invasion (**Figure 8G**). In vivo, simvastatin also antagonized cholesterol-driven tumor growth, as shown by reduced tumor diameter in cholesterol-stimulated A2780 xenografts treated with simvastatin (**Figure S4G**).

At the molecular level, simvastatin treatment led to a significant reduction in ALDH1L2 expression. Western blotting and RT–qPCR confirmed that both ALDH1L2 protein and mRNA levels were markedly decreased after simvastatin treatment in A2780-PM cells (**Figure 8H-I**). Consistently, JC-1 staining revealed that simvastatin disrupted

mitochondrial membrane potential homeostasis (**Figure 8J**). Flow cytometric detection of ROS further showed that simvastatin reversed the cholesterol-induced reduction in intracellular ROS levels, indicating that inhibition of cholesterol synthesis perturbs the mitochondrial redox state of ovarian cancer cells (**Figure 8K**).

At the epigenetic level, simvastatin treatment caused a broad decrease in histone lysine crotonylation and markedly reduced H3K36cr modification levels in A2780-PM cells (**Figure 8L**). ELISA-based detection further confirmed that simvastatin significantly lowered extracellular crotonyl-CoA levels (**Figure 8M**). Moreover, patient-derived organoid assays demonstrated that simvastatin effectively suppressed the growth of ovarian cancer organoids, including both primary and metastatic organoid models (**Figure 8N**).

Mechanistically, simvastatin reduced H3K36cr levels in A2780-PM cells, whereas exogenous cholesterol stimulation enhanced H3K36cr abundance in A2780 cells; this cholesterol-induced increase was reversed by simvastatin treatment (**Figure 8O**). ChIP-qPCR assays further showed that simvastatin abolished H3K36cr enrichment at the ALDH1L2 promoter region (**Figure 8P**), supporting the notion that cholesterol metabolism regulates ALDH1L2 transcription through H3K36 crotonylation. Finally, subcutaneous xenograft analysis demonstrated that simvastatin reduced cholesterol-driven tumor growth, while longitudinal bioluminescence imaging in an intraperitoneal A2780 tumor model further confirmed that simvastatin suppressed intraperitoneal ovarian cancer progression in vivo (**Figure 8Q-R**). Collectively, these findings demonstrate that simvastatin suppresses ovarian cancer malignancy by disrupting the cholesterol–H3K36cr–ALDH1L2 metabolic–epigenetic axis.

4. Discussion

The central finding of this study is that cholesterol metabolism in ovarian cancer is not merely a fuel source but an active upstream regulator of chromatin state. By expanding the intracellular crotonyl-CoA reservoir, hyperactive cholesterol flux selectively deposits H3K36cr at ALDH1L2 enhancers, enabling YY1-driven transcription of a mitochondrial enzyme that sustains redox homeostasis, membrane potential, and oxidative metabolism. This lipid-metabolite-chromatin-transcription-mitochondria relay provides a mechanistic framework

for how systemic metabolic alterations become hardwired into the epigenetic state of metastatic cells.

These findings integrate with and extend prior work on lipid-centric adaptation during ovarian cancer dissemination. Cholesterol homeostasis reflects coordinated synthesis, uptake, efflux, and esterification, with HMGCR and SQLE constraining the rate-limiting steps of de novo synthesis[41]. In the highly invasive A2780-PM subline we established, we observed canonical features of cholesterol metabolic reprogramming relative to parental A2780 cells: increased HMGCR/SQLE expression, higher total cellular cholesterol, and augmented uptake. Crucially, our study elucidates the previously obscure metabolic conversion path from cholesterol metabolic reprogramming to epigenetic remodeling. Hyperactive cholesterol and oxysterol signaling through the LXR–SREBP axis not only boosts de novo lipogenesis but also accelerates global lipid turnover and fatty acid β-oxidation (FAO) [42]. This enhanced lipid catabolism continuously generates massive amounts of short-chain acyl-CoAs, including crotonyl-CoA—a key intermediate in fatty acid and amino acid oxidation[22]. The resulting expansion of the intracellular crotonyl-CoA pool provides abundant non-canonical acyl donors for histone acetyltransferases (such as p300), thereby establishing a direct, substrate-driven biochemical conduit between lipid metabolism and epigenetic histone crotonylation (Kcr) [43]. By positioning cholesterol metabolic reprogramming upstream of crotonyl-CoA expansion and enhancer-proximal H3K36cr deposition, our data connect systemic metabolic adaptations to specific epigenetic states that favor metastatic persistence.

Mechanistically, we identify ALDH1L2 as a downstream mitochondrial effector that sits at the intersection of one-carbon metabolism, redox balance, and mitochondrial membrane potential (Δψ m) [12, 44]. RNA-seq of cholesterol-treated cells nominated ALDH1L2, a mitochondrial enzyme that catalyzes 10-formyltetrahydrofolate deformylation to regenerate tetrahydrofolate with concomitant NADPH production. Consistent with this functional positioning, ALDH1L2 is prominently upregulated in invasive cells and upon exogenous lipid stimulation, but is downregulated following mevalonate-axis inhibition.

Importantly, we outline a rigorous causal relationship within this metabolic-epigenetic cascade: the targeted deposition of H3K36cr functionally remodels the local chromatin accessibility at ALDH1L2 regulatory enhancers, which subsequently dictates and facilitates the recruitment of the transcription factor YY1. This YY1-driven ALDH1L2 activation is not merely a downstream correlation; rather, it functionally mediates the pro-metastatic effects of cholesterol metabolic reprogramming. Loss-of-function experiments indicate that ALDH1L2 depletion impairs Δψm, triggers ROS accumulation, and profoundly diminishes cellular proliferation, migration, and invasion, cementing a “cholesterol metabolic reprogramming–H3K36cr–ALDH1L2” axis that couples aberrant cholesterol metabolism to mitochondrial resilience and metastatic competence.

Because this precise H3K36cr-YY1-ALDH1L2 mechanism functionally orchestrates the malignant phenotypes, the therapeutic implications of intercepting this axis are highly translational. First, enzymes governing cholesterol biogenesis (HMGCR, SQLE) and acyl-CoA metabolism (ACSS2) emerge as actionable nodes, with our data showing that simvastatin and related interventions profoundly attenuate these aggressive phenotypes. Second, given that cholesterol metabolic reprogramming is inextricably coupled to fatty acid oxidation and continuous crotonyl-CoA production, rational combination therapies that pair mevalonate-axis inhibitors (statins) with pharmacological agents that blunt fatty acid oxidation may synergistically and more effectively disrupt the feed-forward loop sustaining enhancer Kcr and pro-metastatic transcriptional programs[45].

Nonetheless, several limitations merit consideration. The A2780/A2780-PM system provides robust mechanistic insights but requires validation across additional patient-derived organoid (PDO) models and in vivo orthotopic metastasis paradigms to establish broader clinical generality. Establishing the absolute necessity and sufficiency of H3K36cr at specific enhancers for ALDH1L2 activation will benefit from locus-targeted epigenome editing (e.g., dCas9-based systems) and quantitative chromatin conformation assays. Furthermore, stable-isotope tracing coupled with targeted metabolomics should

be employed to precisely partition the relative contributions of β-oxidation versus other short-chain acyl sources to the crotonyl-CoA pool under targeted lipid perturbations. Finally, although ALDH1L2 is a compelling effector, unbiased enhancer-centric multi-omics (such as Hi-C integrated with lipidomics) may reveal additional mitochondrial and redox determinants operating within this axis, and spatial epigenomic profiling of matched primary and metastatic clinical specimens could refine patient stratification for future interventions targeting cholesterol metabolic reprogramming.

Conclusion

In summary, we identify a cholesterol–H3K36cr–YY1–ALDH1L2 axis that connects lipid flux to mitochondrial fitness through enhancer-directed epigenetic regulation, providing a mechanistic basis for the association between cholesterol metabolism and ovarian cancer aggressiveness. Pharmacological disruption of this axis with simvastatin—and potentially with agents targeting crotonyl-CoA metabolism—offers a rational entry point for intercepting metabolic‑epigenetic crosstalk in advanced disease.

Declarations

Ethics approval and consent to participate

All experimental procedures involving human and animal subjects were conducted in accordance with the Declaration of Helsinki and relevant institutional guidelines. Human tissue collection was approved by the Ethics Committee of Guangzhou Medical University (Approval No. 2025-023), with written informed consent obtained from all participating patients. Animal experiments were approved by the Institutional Animal Care and Use Committee of Guangzhou Medical University (Approval No. N2025-12067).

Consent for publication

Not applicable.

Availability of data and material

The data that support the findings of this study have been deposited into CNSA[46] with accession number CNP0009417. For any further data requests, please contact the corresponding author.

Competing interests

The authors declare that they have no conflict of interest.

Funding

This work was supported by National Natural Science Foundation [Grant No. 82272985 to Shuo Chen]; Guangzhou Municipal Science and Technology Project [No. 2024A03J0897; 2025A03J3761 to Shuo Chen]; Natural Science Foundation of Guangdong Province [No. 2025A1515012402 to Yang Zhao]; North Sichuan Medical College Affiliated Hospital (2023-2GC010, AW to Ai-ping Wen) and China Foundation for Youth Entrepreneurship and Employment (P250516109033 to Ai-ping Wen).

Authors' contribution

CJC: Software, Conceptualization, Writing – original draft, Visualization, Writing – review & editing. MXJ: Software, Data curation, Writing – review & editing.

JLW: Investigation, Writing – review & editing. JY: Data curation, Writing – review & editing. XCH: Visualization, Data curation. WAP: Supervision, Writing – review & editing. YXH: Software. IL & JK: Writing – review & editing. YZ: Software, Supervision, Writing – review & editing. SC: Funding acquisition, Supervision, Formal analysis, Writing – review & editing.

Declaration of generative AI and AI-assisted technologies in the manuscript preparation process

During the preparation of this work, the author(s) used Gemini for language editing. The author(s) reviewed and edited the output as needed and take full responsibility for the content of the published article.

Acknowledgments

We sincerely thank all the patients who participated in this study and donated tissues for clinical and single-cell transcriptomic analyses. We also acknowledge the contributors and maintainers of the public databases utilized in this study, including GEO, TCGA, and other open-access platforms. We express our gratitude to the Core Facilities at Guangzhou Medical University for excellent technical assistance in animal housing, flow cytometry, and high-throughput sequencing.

Reference

1. Siegel RL, Giaquinto AN, Jemal A. Cancer statistics, 2024. CA: a cancer journal for clinicians. 2024;74(1):12-49.
2. Modugno F, Edwards RP. Ovarian cancer: prevention, detection, and treatment of the disease and its recurrence. Molecular mechanisms and personalized medicine meeting report. International journal of gynecological cancer : official journal of the International Gynecological Cancer Society. 2012;22(8):S45-57.
3. Liu S, Wu M, Wang F. Research Progress in Prognostic Factors and Biomarkers of Ovarian Cancer. Journal of Cancer. 2021;12(13):3976-96.
4. King RJ, Singh PK, Mehla K. The cholesterol pathway: impact on immunity and cancer. Trends in Immunology. 2022;43(1):78-92.
5. Revilla G, Cedó L, Tondo M, Moral A, Pérez JI, Corcoy R, et al. LDL, HDL and endocrine-related cancer: From pathogenic mechanisms to therapies. Seminars in Cancer Biology. 2021;73:134-57.
6. Yarmolinsky J, Bull CJ, Vincent EE, Robinson J, Walther A, Smith GD, et al. Association Between Genetically Proxied Inhibition of HMG-CoA Reductase and Epithelial Ovarian Cancer. Jama. 2020;323(7):646-55.
7. Deng C-M, Zhang G-G, Liu Q-W, Xu J-J, Liu Z-C, Yang J, et al. ANO1 Reprograms Cholesterol Metabolism and the Tumor Microenvironment to Promote Cancer Metastasis. Cancer Research. 2023;83(11):1851-65.
8. Wang X, Lee D, Xu H, Sui Y, Meisenhelder J, Hunter T. PIN1 Prolyl Isomerase Promotes Initiation and Progression of Bladder Cancer through the SREBP2-Mediated Cholesterol Biosynthesis Pathway. Cancer discovery. 2025;15(3):633-55.
9. Yu Y, Ma J, Zhou M, Gu X, Zhou Y, Li Z, et al. NUDT21-mediated Alternative Polyadenylation of CDK19 Reprograms Cholesterol Biosynthesis to Drive Colorectal Cancer Progression. Advanced Science. 2026;13(7):e18346.
10. Huang B, Song B-l, Xu C. Cholesterol metabolism in cancer: mechanisms and therapeutic opportunities. Nature Metabolism. 2020;2(2):132-41.
11. Nelson ER, Wardell SE, Jasper JS, Park S, Suchindran S, Howe MK, et al. 27-Hydroxycholesterol Links Hypercholesterolemia and Breast Cancer Pathophysiology. Science. 2013;342(6162):1094-8.
12. Krupenko NI, Dubard ME, Strickland KC, Moxley KM, Oleinik NV, Krupenko SA. ALDH1L2 is the mitochondrial homolog of 10-formyltetrahydrofolate dehydrogenase. The Journal of biological chemistry. 2010;285(30):23056-63.
13. Hennequart M, Pilley SE, Labuschagne CF, Coomes J, Mervant L, Driscoll PC, et al. ALDH1L2 regulation of formate, formyl-methionine, and ROS controls cancer cell migration and metastasis. Cell reports. 2023;42(6):112562.
14. Li C, Teng P, Sun S, Cui K, Yao S, Fei B, et al. Acetylation of aldehyde dehydrogenase ALDH1L2 regulates cellular redox balance and the chemosensitivity of colorectal cancer to 5-fluorouracil. The Journal of biological chemistry. 2023;299(9):105090.
15. Yang Y, Liu S, Gao H, Wang P, Zhang Y, Zhang A, et al. Ursodeoxycholic acid protects against cisplatin-induced acute kidney injury and mitochondrial dysfunction through acting on ALDH1L2. Free radical biology & medicine. 2020;152:821-37.
16. Weintraub AS, Li CH, Zamudio AV, Sigova AA, Hannett NM, Day DS, et al. YY1 Is a Structural Regulator of Enhancer-Promoter Loops. Cell. 2017;171(7):1573-88.e28.
17. Klemm SL, Shipony Z, Greenleaf WJ. Chromatin accessibility and the regulatory epigenome. Nature

Reviews Genetics. 2019;20(4):207-20.
18. Bannister AJ, Kouzarides T. Regulation of chromatin by histone modifications. Cell Research. 2011;21(3):381-95.
19. Kinnaird A, Zhao S, Wellen KE, Michelakis ED. Metabolic control of epigenetics in cancer. Nature Reviews Cancer. 2016;16(11):694-707.
20. Tan M, Luo H, Lee S, Jin F, Yang Jeong S, Montellier E, et al. Identification of 67 Histone Marks and Histone Lysine Crotonylation as a New Type of Histone Modification. Cell. 2011;146(6):1016-28.
21. Fang Y, Xu X, Ding J, Yang L, Doan MT, Karmaus PWF, et al. Histone crotonylation promotes mesoendodermal commitment of human embryonic stem cells. Cell stem cell. 2021;28(4):748-63.e7.
22. Sabari BR, Tang Z, Huang H, Yong-Gonzalez V, Molina H, Kong HE, et al. Intracellular crotonyl-CoA stimulates transcription through p300-catalyzed histone crotonylation. Molecular cell. 2015;58(2):203-15.
23. Zhao S, Zhang X, Li H. Beyond histone acetylation—writing and erasing histone acylations. Current Opinion in Structural Biology. 2018;53:169-77.
24. Hao Y, Hao S, Andersen-Nissen E, Mauck WM, Zheng S, Butler A, et al. Integrated analysis of multimodal single-cell data. Cell. 2021;184(13):3573-87.e29.
25. Jin S, Guerrero-Juarez CF, Zhang L, Chang I, Ramos R, Kuan C-H, et al. Inference and analysis of cell-cell communication using CellChat. Nature communications. 2021;12(1):1088.
26. Li H, Handsaker B, Wysoker A, Fennell T, Ruan J, Homer N, et al. The Sequence Alignment/Map format and SAMtools. Bioinformatics. 2009;25(16):2078-9.
27. Zhang Y, Liu T, Meyer CA, Eeckhoute J, Johnson DS, Bernstein BE, et al. Model-based Analysis of ChIP-Seq (MACS). Genome Biology. 2008;9(9):R137.
28. Yu G, Wang L-G, He Q-Y. ChIPseeker: an R/Bioconductor package for ChIP peak annotation, comparison and visualization. Bioinformatics. 2015;31(14):2382-3.
29. Tie J, Pan Y, Zhao L, Wu K, Liu J, Sun S, et al. MiR-218 Inhibits Invasion and Metastasis of Gastric Cancer by Targeting the Robo1 Receptor. PLOS Genetics. 2010;6(3):e1000879.
30. Sang X-B, Sun K-X, Wang L-L, Chen S, Wu D-D, Zong Z-H, et al. Effects and mechanism of RhoC downregulation in suppressing ovarian cancer stem cell proliferation, drug resistance, invasion and metastasis. Oncology Reports. 2016;36(6):3267-74.
31. Zheng R, Wan C, Mei S, Qin Q, Wu Q, Sun H, et al. Cistrome Data Browser: expanded datasets and new tools for gene regulatory analysis. Nucleic Acids Research. 2019;47(D1):D729-D35.
32. Zhang Q, Liu W, Zhang H-M, Xie G-Y, Miao Y-R, Xia M, et al. hTFtarget: A Comprehensive Database for Regulations of Human Transcription Factors and Their Targets. Genomics, Proteomics & Bioinformatics. 2020;18(2):120-8.
33. Shen W-K, Chen S-Y, Gan Z-Q, Zhang Y-Z, Yue T, Chen M-M, et al. AnimalTFDB 4.0: a comprehensive animal transcription factor database updated with variation and expression annotations. Nucleic Acids Research. 2023;51(D1):D39-D45.
34. Andersson R, Gebhard C, Miguel-Escalada I, Hoof I, Bornholdt J, Boyd M, et al. An atlas of active enhancers across human cell types and tissues. Nature. 2014;507(7493):455-61.
35. Heinz S, Benner C, Spann N, Bertolino E, Lin YC, Laslo P, et al. Simple Combinations of Lineage-Determining Transcription Factors Prime cis-Regulatory Elements Required for Macrophage and B Cell Identities. Molecular cell. 2010;38(4):576-89.
36. Jin X, Demere Z, Nair K, Ali A, Ferraro GB, Natoli T, et al. A metastasis map of human cancer cell lines. Nature. 2020;588(7837):331-6.

37. Hölttä-Vuori M, Uronen R-L, Repakova J, Salonen E, Vattulainen I, Panula P, et al. BODIPY-Cholesterol: A New Tool to Visualize Sterol Trafficking in Living Cells and Organisms. Traffic. 2008;9(11):1839-49.
38. Li Y, Sabari BR, Panchenko T, Wen H, Zhao D, Guan H, et al. Molecular Coupling of Histone Crotonylation and Active Transcription by AF9 YEATS Domain. Molecular cell. 2016;62(2):181-93.
39. Li L, Xiang T, Guo J, Guo F, Wu Y, Feng H, et al. Inhibition of ACSS2-mediated histone crotonylation alleviates kidney fibrosis via IL-1β-dependent macrophage activation and tubular cell senescence. Nature communications. 2024;15(1):3200.
40. Xiong X, Panchenko T, Yang S, Zhao S, Yan P, Zhang W, et al. Selective recognition of histone crotonylation by double PHD fingers of MOZ and DPF2. Nature chemical biology. 2016;12(12):1111-8.
41. Mullen PJ, Yu R, Longo J, Archer MC, Penn LZ. The interplay between cell signalling and the mevalonate pathway in cancer. Nature Reviews Cancer. 2016;16(11):718-31.
42. Cheng C, Geng F, Cheng X, Guo D. Lipid metabolism reprogramming and its potential targets in cancer. Cancer Communications. 2018;38(1):27.
43. Sivanand S, Viney I, Wellen KE. Spatiotemporal Control of Acetyl-CoA Metabolism in Chromatin Regulation. Trends in Biochemical Sciences. 2018;43(1):61-74.
44. Piskounova E, Agathocleous M, Murphy MM, Hu Z, Huddlestun SE, Zhao Z, et al. Oxidative stress inhibits distant metastasis by human melanoma cells. Nature. 2015;527(7577):186-91.
45. Ma X, Bi E, Lu Y, Su P, Huang C, Liu L, et al. Cholesterol Induces CD8⁺ T Cell Exhaustion in the Tumor Microenvironment. Cell metabolism. 2019;30(1):143-56.e5.
46. Weiwen Wang, et al. The China National GeneBank Sequence Archive (CNSA) 2024 update, Horticulture Research, Volume 12, Issue 5, May 2025, uhaf036, https://doi.org/10.1093/hr/uhaf036

Table 1. Serum lipid profile in ovarian cancer patients by FIGO stage

Variable	FIGO I-II(n=50)	FIGO III–IV (n=68)	P-value
Age (years) Average	51.64	53.55	0.5282
TC (mmol/L) Average	4.14	4.98	<0.0001*
TG (mmol/L) Average	1.57	1.44	0.9875

Notes: Asterisk indicates statistical significance at P<0.05

Abbreviations: TC, total cholesterol; TG, triglycerides.

Data are presented as mean. Serum lipid parameters were collected from 118 patients (FIGO I–II, n = 50; FIGO III–IV, n = 68) at the affiliated hospital of Guangzhou Medical University. TC, total cholesterol; TG, triglycerides. P-values were calculated by two-sided Student's *t*-test. *P < 0.05 was considered statistically significant. Individual patient-level data are provided in Table S1.

Table 2. Subset analysis: patients with apolipoprotein-related laboratory results available

Variable	FIGO I-II(n=31)	FIGO III-IV(n=58)	P-value
Age (years) Average	50.58	53.78	0.4123
HDL (mmol/L) Average	1.23	1.24	>0.9999
LDL (mmol/L) Average	2.68	3.24	0.0043*

Notes: Asterisk indicates statistical significance at P<0.05

Abbreviations: HDL, high-density lipoprotein; LDL, low-density lipoprotein.

Data are presented as mean. A subset of 89 patients (FIGO I–II, n = 31; FIGO III–IV, n = 58) from the full cohort had additional apolipoprotein-related lipid parameters available. HDL, high-density lipoprotein cholesterol; LDL, low-density lipoprotein cholesterol. P-values were calculated by two-sided Student's *t*-test. *P < 0.05 was considered statistically significant.

Figure 1. Enhanced cholesterol biosynthesis in metastatic ovarian cancer promotes tumor progression and modulates the tumor microenvironment.

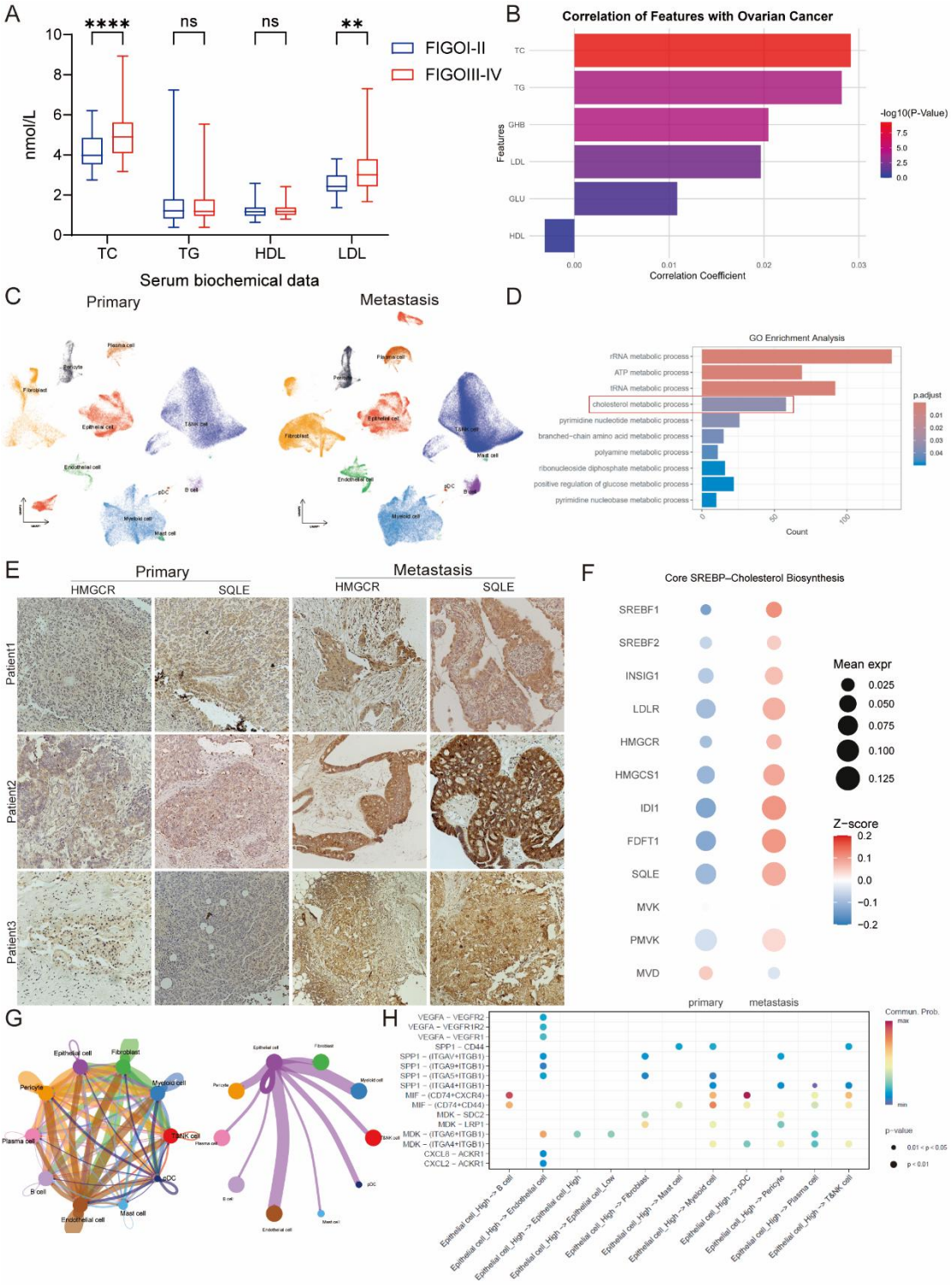

(a) Box plots of serum TC, TG, HDL and LDL levels in patients with early-stage (FIGO I–II) versus advanced-stage (FIGO III–IV) ovarian cancer. (b) Bar plot of correlation coefficients between clinical metabolic features and ovarian cancer. (c) UMAP plots of the single-cell atlas of primary and metastatic ovarian cancer, coloured by cell type. (d) GO enrichment analysis of differentially expressed genes in metastatic tumour cells. (e) Representative IHC images of HMGCR and SQLE expression in paired primary and metastatic tumour tissues from three patients. (f) Dot plot of expression patterns of core SREBP-mediated cholesterol biosynthesis genes in primary and metastatic lesions. (g) Circle plots of global cell–cell communication networks in

883 the tumour microenvironment and epithelial cell-derived signalling interactions. (h) Dot plot of significant ligand–receptor
884 interactions between high-metabolic epithelial cells and surrounding immune or stromal cells.

Figure 2. Establishment and characterization of the highly invasive A2780-PM ovarian cancer cell line with enhanced cholesterol metabolism and angiogenic potential.

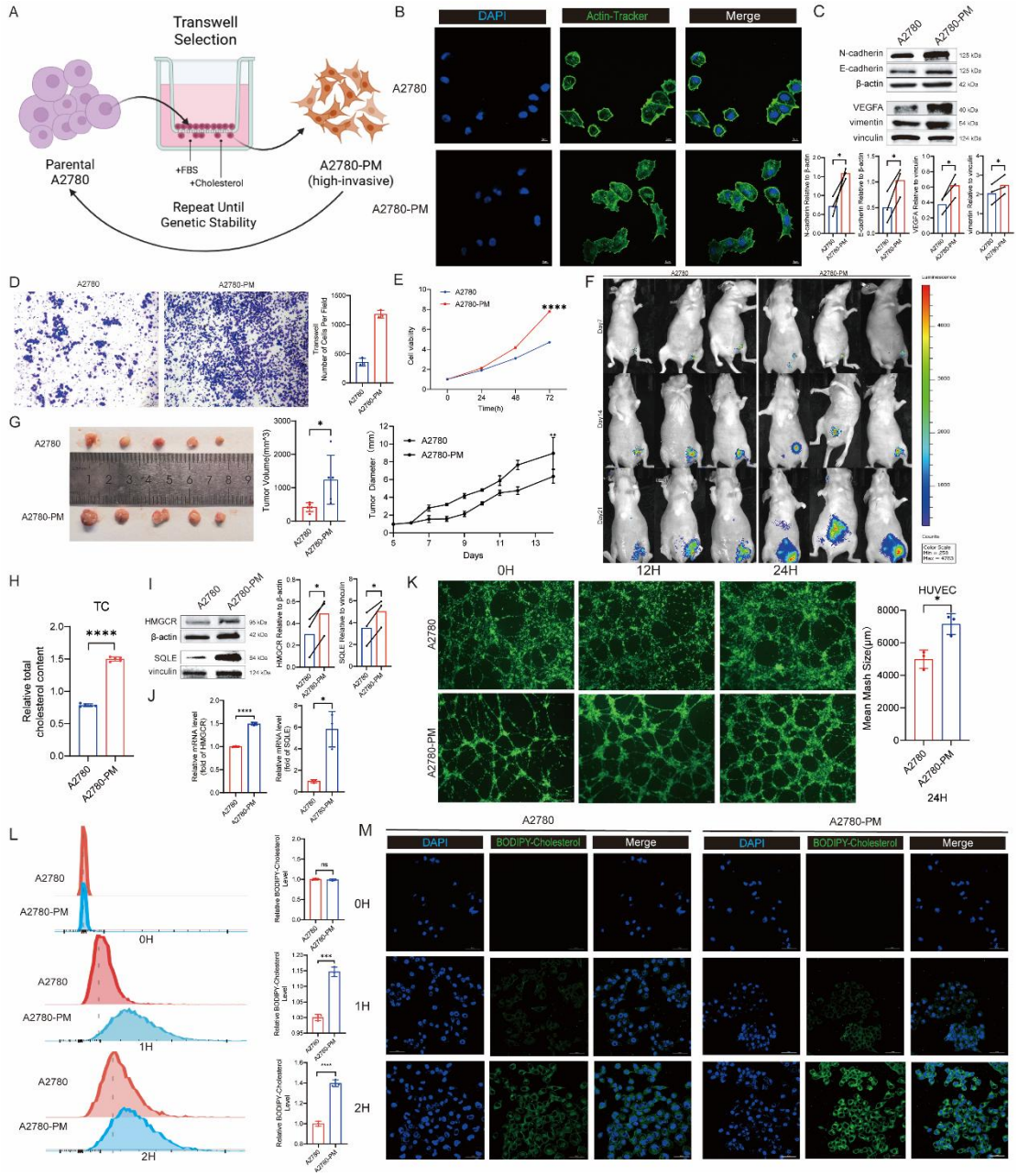

(a) Schematic of the generation of the highly invasive A2780-PM subline from parental A2780 cells by repeated Transwell selection with FBS and cholesterol. (b) Representative confocal immunofluorescence images of morphological changes in A2780 and A2780-PM cells; F-actin stained with Actin-Tracker (green), nuclei with DAPI (blue). (c) Western blot of EMT markers (N-cadherin, E-cadherin, vimentin) and invasion/angiogenesis-related proteins (VEGFA, MMP2) in A2780 and A2780-PM cells; β-actin and vinculin, loading controls. (d) Representative images and quantification of Transwell invasion assays of A2780 and A2780-PM cells. (e) CCK-8 assay of cell viability and proliferation in A2780 and A2780-PM cells at 0, 24, 48 and 72 h. (f) Representative bioluminescence images of mice bearing xenograft tumours derived from A2780 or A2780-PM cells. (g) Representative images of excised subcutaneous tumours, tumour volume quantification and tumour growth curves of A2780- and A2780-PM-derived xenografts. (h) Relative intracellular total cholesterol content in A2780 and A2780-PM cells. (i) Protein and relative mRNA levels of cholesterol synthesis enzymes HMGCR and SQLE in A2780 and A2780-PM cells, determined by western blotting and RT–qPCR. (j) Representative images and quantification of HUVEC tube formation after treatment with conditioned medium from A2780 or A2780-PM cells. (k) Flow cytometric analysis of time-dependent BODIPY-cholesterol

uptake in A2780 and A2780-PM cells at 0, 1 and 2 h. (l) Representative confocal images of time-dependent cellular uptake of BODIPY-cholesterol (green) in A2780 and A2780-PM cells; nuclei stained with DAPI (blue).

Figure 3. Cholesterol enhances the malignant phenotypes of ovarian cancer cells, whereas targeted inhibition of cholesterol biosynthesis exerts anti-tumor effects.

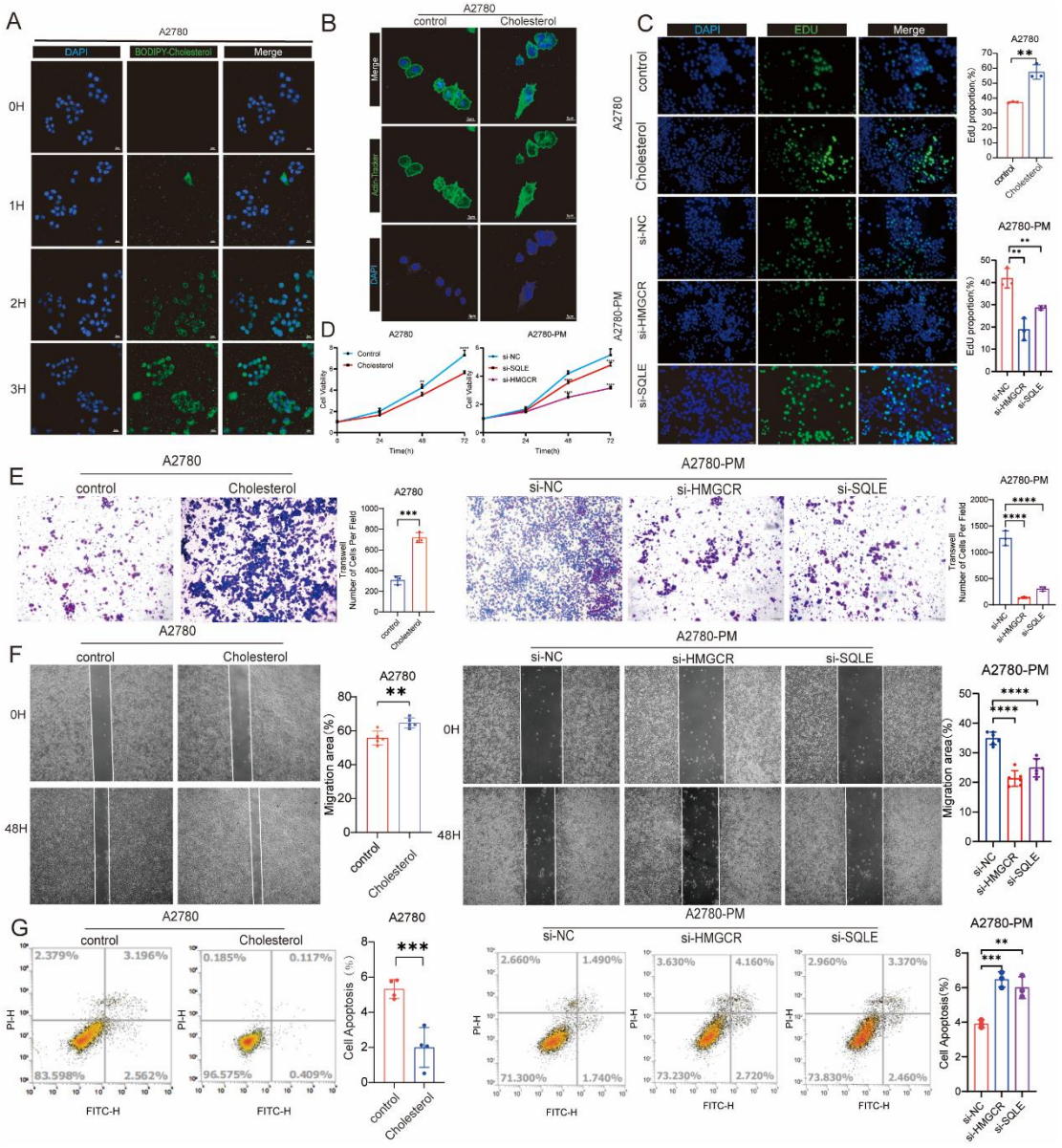

(a) Representative confocal immunofluorescence images of time-dependent cellular uptake of BODIPY-labelled cholesterol (green) in A2780 cells; nuclei counterstained with DAPI (blue). (b) Fluorescence images of Actin-Tracker staining (green) revealing cytoskeletal remodelling in A2780 cells following cholesterol treatment. (c) EdU incorporation assays of cell proliferation. Left: A2780 cells treated with or without exogenous cholesterol. Right: A2780-PM cells transfected with si-NC, si-HMGCR or si-SQLE. Representative images and corresponding quantification of the EdU-positive proportion are shown. (d) Cell viability measured over 72 h in the indicated A2780 and A2780-PM cell models. (e) Transwell assays of invasive capacity in A2780 cells (cholesterol-treated) and A2780-PM cells (HMGCR or SQLE knockdown). Representative crystal violet staining images and quantitative cell counts per field are shown. (f) Wound-healing assays of migratory ability of the indicated cells at 0 and 48 h. Bar graphs show statistical analysis of relative migration area. (g) Flow cytometric analysis of apoptosis by Annexin V-FITC and PI double staining. Exogenous cholesterol attenuated basal apoptosis in A2780 cells (left), whereas silencing HMGCR or SQLE triggered significant apoptosis in A2780-PM cells (right).

Figure 4. ALDH1L2 is identified as a cholesterol-driven downstream target regulating mitochondrial metabolism and tumor progression in ovarian cancer.

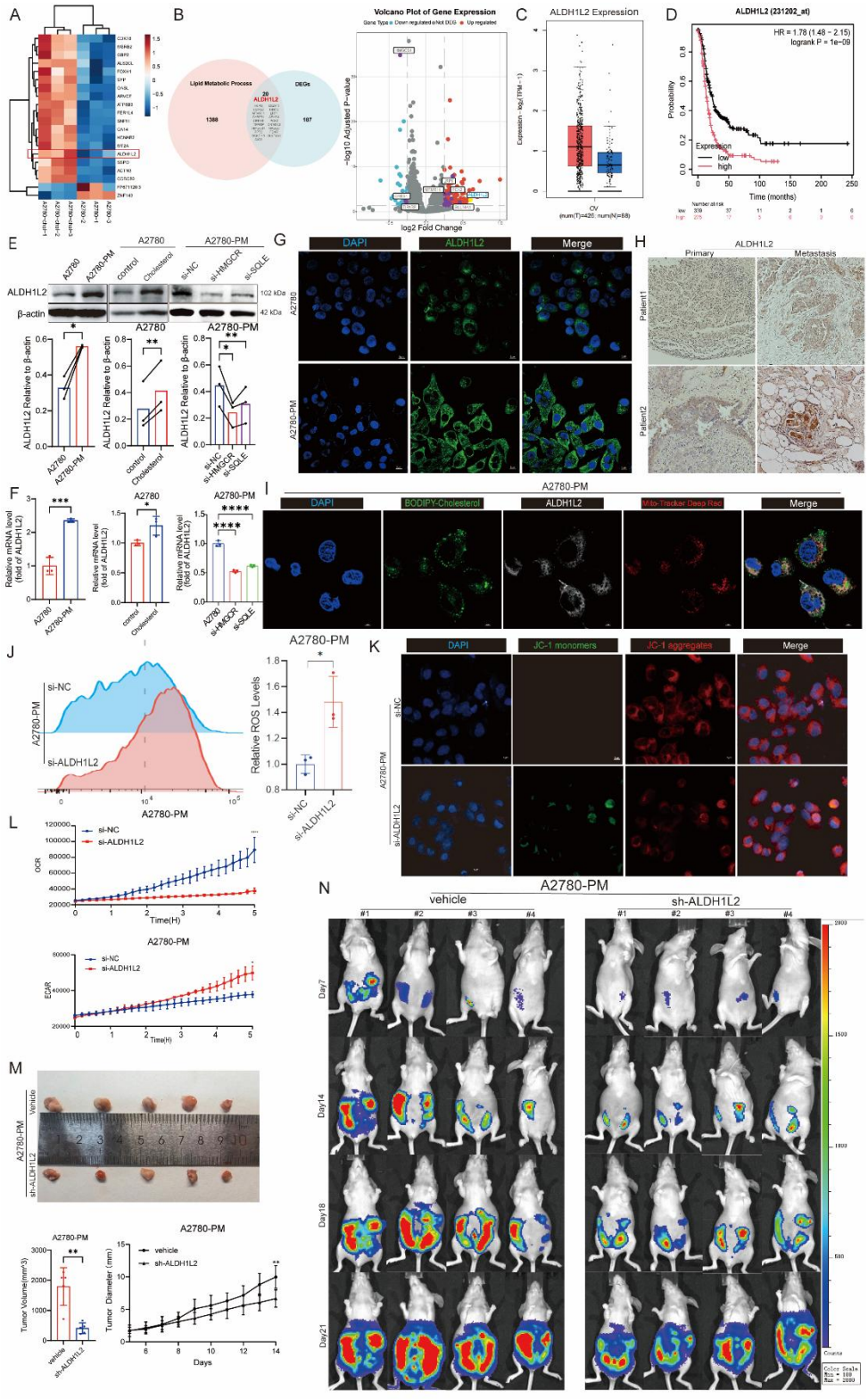

(a) Heatmap of differential expression of lipid metabolism-related genes in primary and metastatic ovarian cancer samples. (b) Intersection and differential expression analyses identifying ALDH1L2 as a candidate gene associated with lipid metabolic reprogramming and metastasis. (c) ALDH1L2 expression in ovarian cancer tissues from public transcriptomic datasets. (d) Kaplan–Meier analysis of the association between ALDH1L2 expression and overall survival in ovarian cancer patients. (e) Western blot and quantification of ALDH1L2 protein expression in A2780 and A2780-PM cells following ALDH1L2 knockdown

or SQLE inhibition. (f) RT–qPCR analysis of ALDH1L2 expression in A2780 and A2780-PM cells under the indicated treatments. (g) Representative immunofluorescence images of ALDH1L2 expression in A2780 and A2780-PM cells. (h) Representative IHC staining of ALDH1L2 in paired primary and metastatic ovarian cancer tissues. (i) Confocal images of subcellular distribution of BODIPY-cholesterol, ALDH1L2 and MitoTracker-labelled mitochondria in A2780-PM cells. (j) Flow cytometric analysis of ROS levels in A2780-PM cells after ALDH1L2 knockdown. (k) JC-1 staining of mitochondrial membrane potential changes in A2780-PM cells following ALDH1L2 knockdown. (l) Real-time metabolic analysis of oxygen consumption rate and extracellular acidification rate in A2780-PM cells after ALDH1L2 knockdown. (m) Subcutaneous xenograft growth of A2780-PM cells with or without ALDH1L2 knockdown. (n) Longitudinal bioluminescence imaging showing that ALDH1L2 knockdown suppresses intraperitoneal tumour progression in mice bearing A2780-PM tumours.

Figure 5. Cholesterol-induced chromatin remodeling promotes ALDH1L2 transcription via the transcription factor YY1.

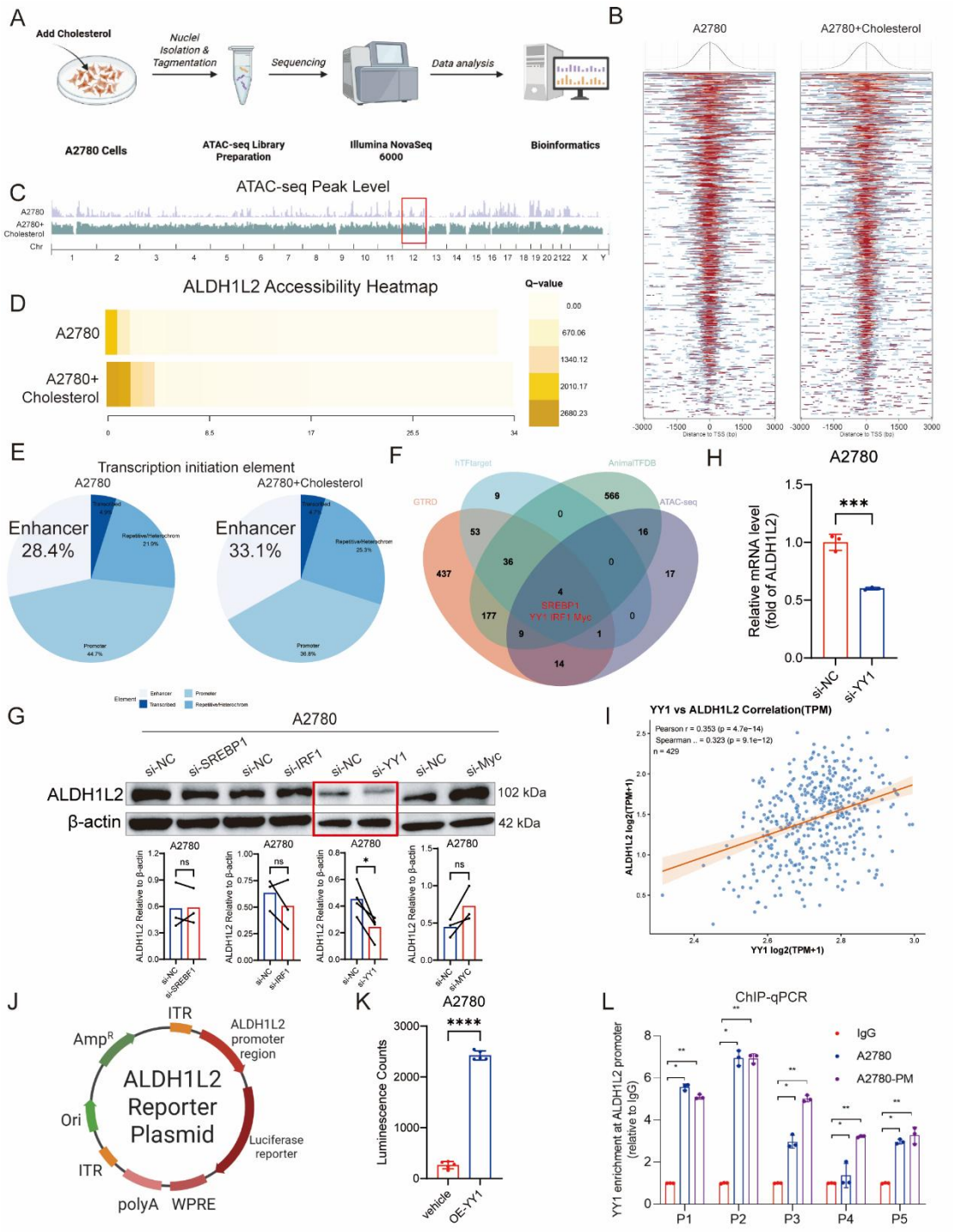

(a) ATAC-seq workflow in A2780 cells treated with or without cholesterol. (b) Heatmaps and average ATAC-seq signal profiles centred on transcription start sites (TSS; ±3 kb). (c) Genome browser tracks of ATAC-seq peaks across chromosomes; red box, region of interest. (d) Differential chromatin accessibility (Q-value) at the ALDH1L2 locus. (e) Genomic distribution of ATAC-seq peaks (promoter, enhancer, transcribed region, repetitive/heterochromatin). (f) Venn diagram intersecting ATAC-seq motif analysis with hTFtarget, AnimalTFDB and GTRD databases, identifying SREBP1, YY1, IRF1 and MYC as candidate upstream transcription factors. (g) Western blot of ALDH1L2 in A2780 cells after siRNA knockdown of the four candidates; β-actin, loading control. (h) ALDH1L2 mRNA levels (RT–qPCR) in A2780 cells transfected with si-NC or si-YY1. (i) Positive correlation between YY1 and ALDH1L2 mRNA expression ($\log_2$(TPM+1)) in a clinical cohort (n = 429); Pearson and Spearman coefficients shown. (j) Dual-luciferase reporter assay of ALDH1L2 promoter activity in A2780 cells co-transfected with vehicle or YY1

overexpression (OE-YY1) plasmid. (k) ChIP–qPCR of YY1 enrichment at five putative binding regions (P1–P5) in the ALDH1L2 promoter in A2780 and A2780-PM cells; IgG, negative control.

*Data are mean ± SD; n = 3 independent experiments. **P < 0.01, ***P < 0.001, ****P < 0.0001.

Figure 6. Cholesterol upregulates ALDH1L2 transcription through YY1-mediated activation of specific upstream enhancers.

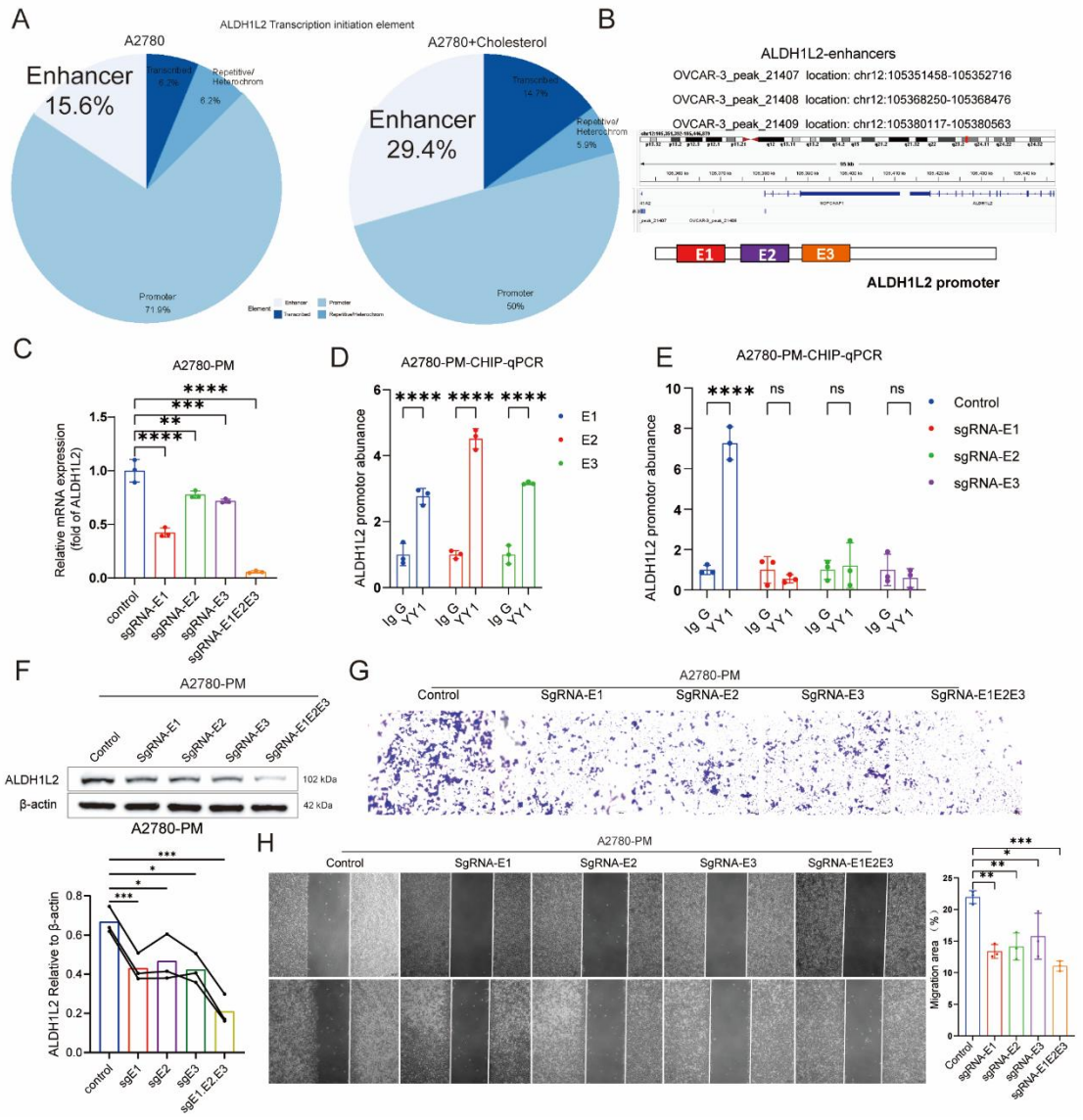

(a) Pie charts showing the distribution of annotated genomic elements. (b) Schematic representation of the genomic locus of ALDH1L2 on chromosome 12, highlighting three identified upstream enhancer regions (E1, E2, and E3) and their respective genomic coordinates. (c) RT–qPCR analysis of ALDH1L2 mRNA expression in A2780-PM cells following CRISPR/sgRNA-mediated targeting of control, individual enhancers (sgRNA-E1, E2, E3), or combined enhancers (sgRNA-E1E2E3). (d) ChIP–qPCR analysis evaluating the binding enrichment of the transcription factor YY1 at the ALDH1L2 regulatory regions (E1, E2, E3) in A2780-PM cells; IgG, negative control. (e) ChIP–qPCR analysis showing the abrogation of YY1 binding to the ALDH1L2 promoter following sgRNA-mediated disruption of the respective enhancers. (f) Representative images and quantification of Transwell invasion assays in A2780-PM cells transfected with control or the indicated enhancer-targeting sgRNAs. (g) Wound-healing migration assays in A2780-PM cells transfected with control or the indicated enhancer-targeting sgRNAs. (h) Western blot validating the downregulation of ALDH1L2 protein levels in A2780-PM cells upon sgRNA-mediated disruption of individual or combined enhancers; β-actin, loading control.

*Data are mean ± SD; n = 3 independent experiments.

Figure 7. Cholesterol-derived crotonyl-CoA drives ALDH1L2 transcription via histone H3K36 crotonylation.

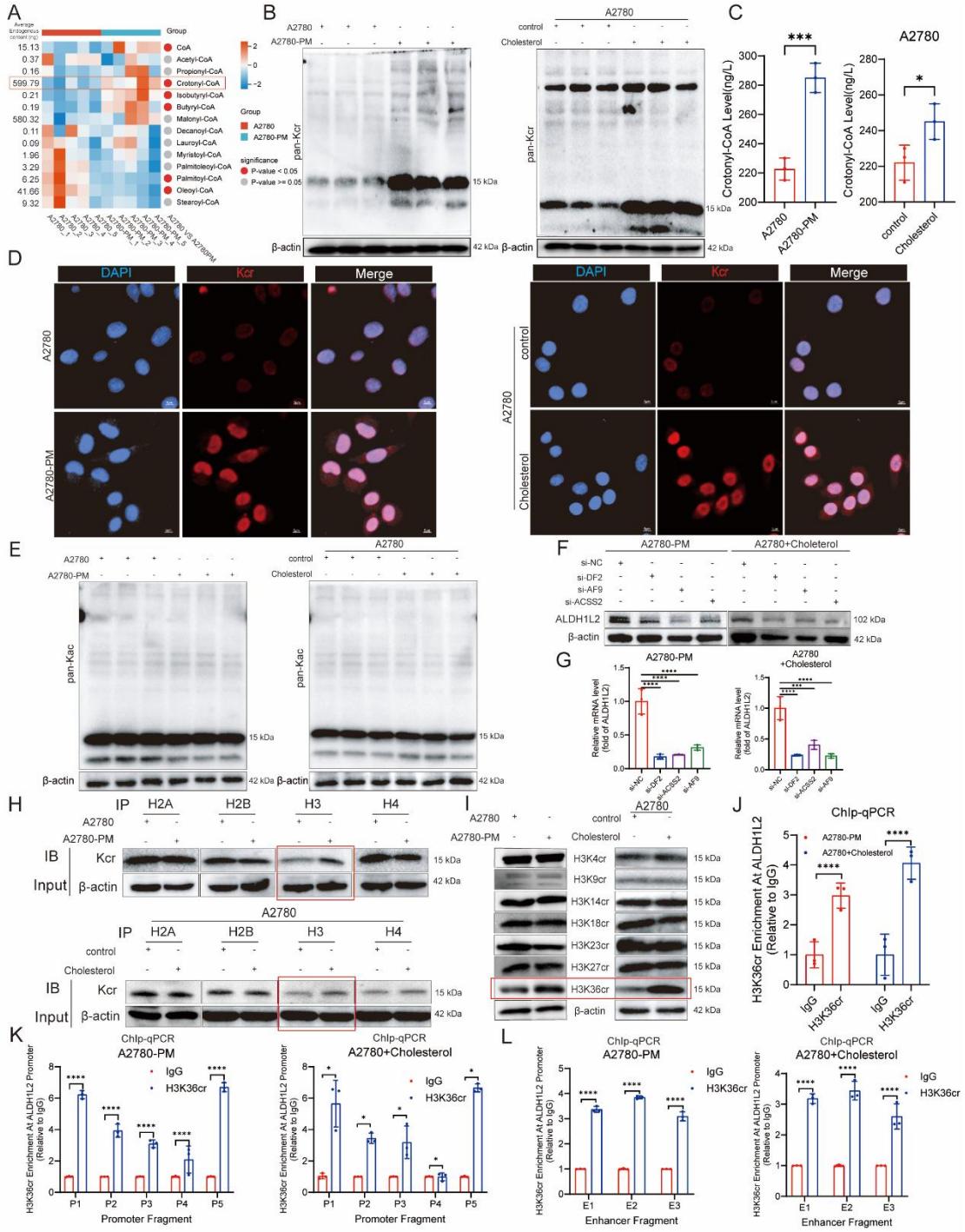

(a) Heatmap of targeted short-chain acyl-CoA metabolomics showing the relative abundance of various acyl-CoAs in A2780 and A2780-PM cells; crotonyl-CoA is highlighted by a red box as the most significantly upregulated metabolite. (b) Western blot of global pan-crotonylation (pan-Kcr) levels in A2780 and A2780-PM cells (left), and A2780 cells treated with or without exogenous cholesterol (right). (c) Quantification of intracellular crotonyl-CoA levels in the indicated cell models, measured by ELISA. (d) Representative confocal immunofluorescence images. (e) Western blot of global pan-acetylation (pan-Kac) levels in the indicated cells. (f) Western blot of ALDH1L2 expression. (g) RT–qPCR analysis of ALDH1L2 relative mRNA expression. (h) Immunoprecipitation of core histones (H2A, H2B, H3, H4) followed by immunoblotting with a pan-Kcr antibody. (i) Western blot screening of specific lysine crotonylation sites on histone H3. (j) ChIP–qPCR analysis showing the overall enrichment of H3K36cr at the ALDH1L2 genomic locus. (k, l) Detailed ChIP–qPCR analysis evaluating the specific enrichment of H3K36cr at

the defined promoter fragments (P1–P5) (k) and enhancer fragments (E1–E3) (l) of the ALDH1L2 gene in the indicated cell models.

*Data are mean ± SD; n = 3 independent experiments.

Figure 8. Genetic mutation of H3K36 or pharmacological inhibition of cholesterol biosynthesis effectively abrogates the H3K36cr/ALDH1L2 axis and suppresses ovarian cancer progression.

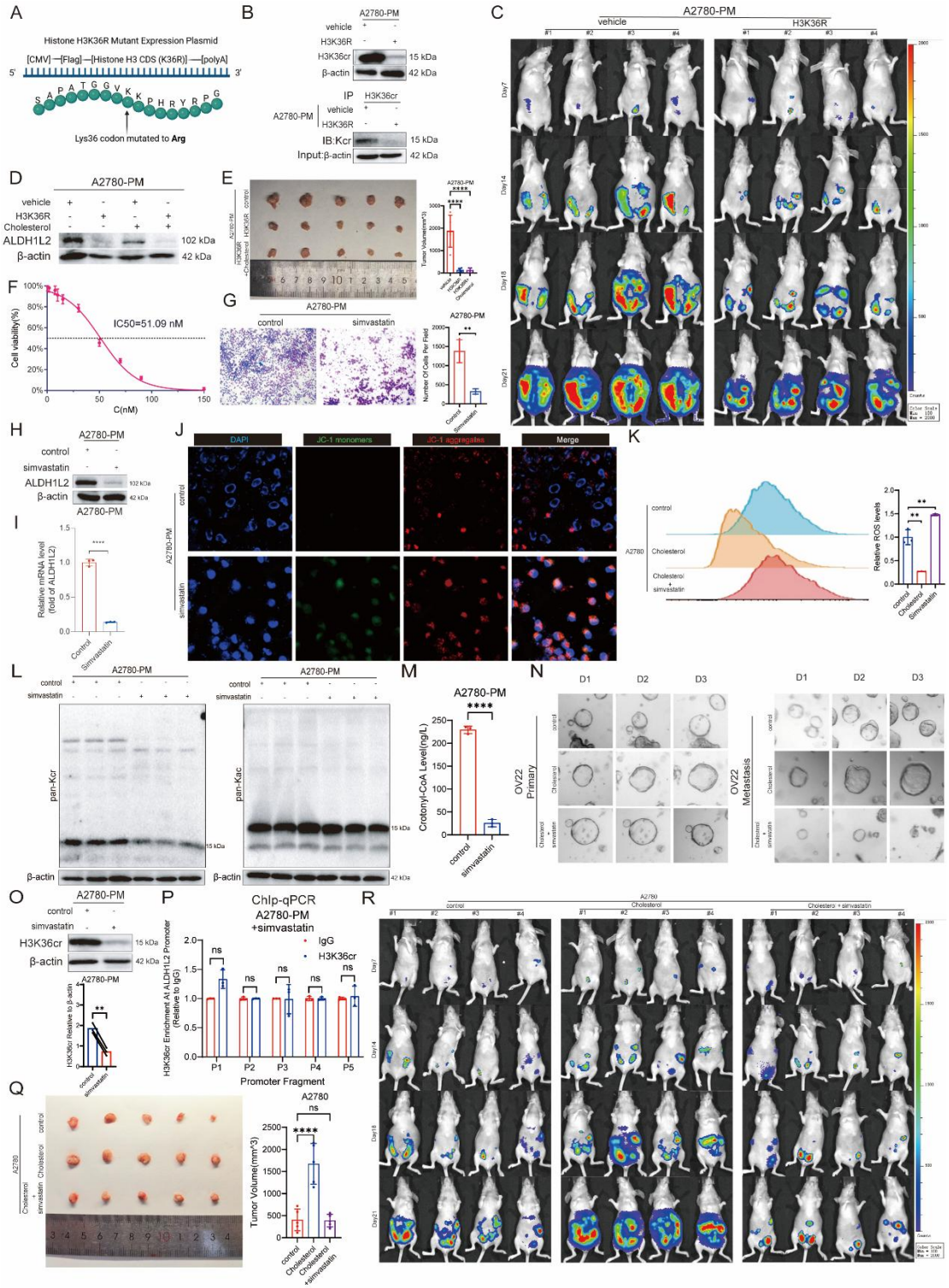

(a) Schematic of the H3K36R mutant histone H3 plasmid, in which lysine 36 is substituted by arginine to block H3K36 crotonylation. (b) Western blot and immunoprecipitation analyses showing reduced H3K36 crotonylation in A2780-PM cells expressing H3K36R. (c) Longitudinal bioluminescence imaging of intraperitoneal A2780-PM tumours expressing vehicle control or H3K36R. (d) Western blot showing that H3K36R reduces ALDH1L2 expression in A2780-PM cells, with or without cholesterol supplementation. (e) Images and quantification of subcutaneous tumours formed by A2780-PM cells expressing vehicle or

H3K36R, with or without cholesterol supplementation. (f) Dose–response curve of the inhibitory effect of simvastatin on A2780-PM cell viability and the calculated IC_{50} value. (g) Representative Transwell images and quantification showing reduced invasion of A2780-PM cells after simvastatin treatment. (h) Western blot showing decreased ALDH1L2 protein expression in A2780-PM cells after simvastatin treatment. (i) RT–qPCR analysis showing reduced ALDH1L2 mRNA expression in A2780-PM cells after simvastatin treatment. (j) JC-1 staining showing altered mitochondrial membrane potential in A2780-PM cells after simvastatin treatment. (k) Flow cytometric analysis of ROS levels in control, cholesterol-treated and cholesterol plus simvastatin-treated A2780 cells. (l) Western blot of global lysine crotonylation and H3K36cr levels in A2780-PM cells after simvastatin treatment. (m) ELISA-based quantification of extracellular crotonyl-CoA levels in A2780-PM cells after simvastatin treatment. (n) Representative images of patient-derived ovarian cancer organoids treated with control, cholesterol or simvastatin. (o) Western blot showing H3K36cr changes in A2780-PM cells after simvastatin treatment. (p) ChIP–qPCR analysis of H3K36cr enrichment at the ALDH1L2 promoter in A2780-PM cells after simvastatin treatment. (q) Images and quantification of subcutaneous A2780 tumours treated with control, cholesterol or cholesterol plus simvastatin. (r) Longitudinal bioluminescence imaging of intraperitoneal A2780 tumours treated with control, cholesterol or cholesterol plus simvastatin.

*Data are mean ± SD; n = 3 independent experiments. **P < 0.01, ***P < 0.001, ****P < 0.0001.

Supplementary Files

This is a list of supplementary files associated with this preprint. Click to download.

- supplementinformation.docx
- supplementaryfile.pdf
- Tables3.xlsx